Applied Thermal Engineering 260 (2025) 124870

Contents lists available at ScienceDirect

Applied Thermal Engineering

journal homepage: www.elsevier.com/locate/ate

Research Paper

Optimisation of a converging-diverging nozzle for the wet-to-dry expansion of the siloxane MM

Pawel Ogrodniczak [a], Abdulnaser Sayma [b], Martin T. White [a,c,*]

[a] Thermo-Fluids Research Centre, School of Science & Technology, City, University of London, Northampton Square, London, EC1V 0HB, UK
[b] College of Engineering, Design and Physical Science, Brunel University London, Uxbridge, Middlesex, UB8 3PH, UK
[c] Energy and Materials Engineering Research Centre, School of Engineering and Informatics, University of Sussex, Falmer, Brighton, BN1 9RH, UK

ARTICLE INFO

Keywords:
Two-phase expansion
Wet-to-dry cycle
Flash boiling
Organic Rankine cycle
Non-equilibrium flow

ABSTRACT

Wet-to-dry expansion within the nozzle guide vane of an ORC turbine has been proposed as a means to improve the power output of ORC systems for waste-heat recovery (< 250 °C). However, given the rapid fluid acceleration in the stator, the phases can develop significant velocity and temperature disparity due to density difference and finite rate of interphase heat transfer. Since these factors can significantly affect the phase-change process, wet-to-dry nozzle design techniques must account for non-equilibrium effects. The first part of this paper aims to further verify a previously developed quasi-1D inviscid non-equilibrium nozzle design tool by comparing it to non-equilibrium CFD simulations, which, unlike the design model, account for lateral flow variations, viscous and turbulence effects, along with secondary momentum forces. Within the CFD model, the interphase mass, momentum, and energy exchange models have been updated using correlations better tailored to evaporating droplet flows and a corrected drag equation. Moreover, the definition of the vapour mass fraction has been modified, while a simplified droplet breakup model has been used to predict the droplet size. The results from the CFD simulations indicate that the outlet vapour mass fraction is approximately 10 to 15% lower than that predicted by the quasi-1D tool. However, the overall flow behaviour and phase-change pattern were in satisfactory agreement, justifying the use of the design tool for 1D optimisation. As such, the quasi-1D tool is coupled to a gradient-based optimiser to optimise the nozzle pressure profile and enhance evaporation of siloxane MM for expansions with an inlet pressure ranging from 450 to 650 kPa, and inlet vapour quality of 0.3. CFD simulations of the optimised geometries indicate an increase of 3.3 to 5.7% in the outlet vapour mass fraction, which was raised from 84.9, 87.7 and 90.5% to 88.2, 93.4 and 95.7% for 450, 550 and 650 kPa inlet pressures respectively. However, a more abrupt expansion in the optimised nozzles resulted in the development of a shock and led to deterioration in nozzle efficiency compared to the baseline nozzles. Finally, a CFD-based shape optimisation was conducted, which demonstrated that it may be difficult to further enhance the vapourisation rate. However, the optimised geometry did mitigate the effect of the oblique shock that appears in the diverging section of the nozzle, raising the expansion efficiency by around 3%.

1. Introduction

In an effort to improve the performance of organic Rankine cycle (ORC) systems, several novel cycle architectures have been proposed [1]. Among the proposed cycles, the so-called *wet-to-dry cycle* could be capable of generating up to 30% more power than a conventional single-phase ORC for heat-source temperatures between 150 and 250 °C [2]. In the wet-to-dry cycle, it is hypothesised that a two-phase mixture of molecularly complex working fluids, such as siloxanes, can be completely vapourised during expansion within the turbine stator, through the process of flash boiling. This offers greater flexibility in terms of expander selection compared to two-phase cycles where the expansion process remains within the saturation dome since turbomachines could be employed. This is provided that complete mixture evaporation occurs in the stator, thus avoiding possible concerns related to erosion of the rotor. Turbomachines also offer higher expansion ratios than volumetric expanders, allowing the application of the wet-to-dry cycle at temperatures above 150 °C. Moreover, having a turbine that could accept two-phase inlet conditions could be an advantage in terms of the off-design operation of ORC systems [3].

* Corresponding author.
E-mail addresses: pawel.ogrodniczak@city.ac.uk (P. Ogrodniczak), martin.white@sussex.ac.uk (M.T. White).

https://doi.org/10.1016/j.applthermaleng.2024.124870
Received 1 February 2024; Received in revised form 10 October 2024; Accepted 7 November 2024
Available online 17 November 2024

The successful design of a wet-to-dry turbine depends on the capability of the stator to facilitate complete mixture evaporation and avoid liquid droplets entering the rotor. To the best knowledge of the authors, there have been no experimental tests, and subsequently no experimental datasets that could be used to validate the concept. Instead the concept has been assessed using numerical tools. A two-phase mixture entering a wet-to-dry nozzle begins to vapourise due to the pressure drop associated with the fluid acceleration in the streamwise direction. This is widely known as flash boiling or flashing, and accurately modelling such flows is essential for designing a wet-to-dry nozzle.

1.1. Numerical simulation of flashing flows

Flashing is a similar phenomenon to cavitation, but phase change is considered to be dominated by the interphase heat transfer, while the effect of pressure non-equilibrium is deemed of secondary importance [4]. Numerical modelling of flashing is a complex task, which requires simultaneous modelling of the liquid and vapour phases, alongside prediction of mass, momentum, and energy exchanges between the phases. In reality, two-phase expansion processes are characterised by finite rates of heat and momentum transfer, which adds to the complexity of the task, as the two phases can develop disparity in velocities (inhomogeneous flow) and temperatures (thermal non-equilibrium flow); these are commonly referred to as non-equilibrium effects.

Several models have been proposed to model flashing flows. The most simplistic approach is the homogeneous-equilibrium model, which assumes the liquid and vapour phases remain at saturation conditions, have an equal velocity, and the mixture behaves as a pseudo-single fluid. However, early experiments on flash boiling of subcooled or saturated water [5] demonstrated that there is a considerable delay in the onset of vapourisation, which did not occur instantaneously when the fluid reached the saturation pressure. In order to account for this delay, a homogeneous-relaxation model was proposed by Bilicki & Kestin [6], which introduces an additional equation, based on an empirically-derived relaxation time, that enables the local vapour mass fraction to deviate from the thermodynamic equilibrium value. Several studies have been carried out to derive the relaxation time for different working fluids, including water [7], carbon dioxide [8,9] and R410a [10] in various applications. Ultimately, these studies show the ability of the homogeneous-relaxation model to better predict mass-flow rate than the homogeneous equilibrium model, but they also demonstrate the importance of having suitable experimental data to tune the relaxation time to the specific working fluid and operating conditions. Another homogeneous non-equilibrium model is the delayed equilibrium model, which treats the mixture as a composition of three phases: saturated liquid, saturated vapour, and a metastable liquid phase. The rate at which the metastable liquid evaporates is defined by three empirical coefficients. De Lorenzo et al. [11] found that the delayed equilibrium model could more reliably predict critical mass-flow rate and pressure in different types of channels compared to other existing flashing models. Recently, Tammone et al. [12] extended the delayed equilibrium model to the flashing of refrigerant R134a, and found the model was capable of predicting the mass-flow rate with an average uncertainty of 6.1% once the model was tuned to the available experimental data. Ultimately, these models can be used to accurately simulate flash boiling problems, assuming that suitable experimental data is available to tune the semi-empirical correlations to the given fluid and operating conditions.

As already mentioned, no suitable experimental data currently exist for the fluids and operating conditions relevant to the wet-to-dry cycle, which emphasises the need for a more general modelling approach that could be applied to a wider range of applications without specific semi-empirical coefficients. Moreover, the homogeneous-relaxation and delayed equilibrium models have originally been developed assuming a negligible impact of mechanical non-equilibrium on the phase change process. However, previous investigations carried out by the authors [13] indicate that the two-phase flow can be highly inhomogeneous under conditions relevant to the wet-to-dry cycle; liquid and vapour phases experience significant velocity slip and separation. Hence, in the context of wet-to-dry expansion, both thermal and mechanical non-equilibrium effects should be taken into account.

A more general modelling technique is based on the non-equilibrium two-fluid model, which employs the Eulerian-Eulerian framework to model both phases as interpenetrating continua. Separate governing equations are solved for liquid and vapour phases so that both thermal and mechanical equilibrium effects are considered. The coupling between the phases, defined in terms of mass, momentum and energy exchange, is accounted for via interphase models, which account for the interfacial forces and interphase heat transfer that defines the vapourisation rate. One of the challenges in implementing the two-fluid model lies in the selection of appropriate interphase models. Although, these are derived empirically, they are not as fine-tuned as the empirical coefficients used in the homogeneous-relaxation and delayed equilibrium models, which allows the application of the two-fluid model without experimental data specific to the investigated flow. However, a challenge lies in the determination of the interfacial area, and different approaches have been used for estimating this, ranging from a simple assumption of a constant diameter [14] or number of the dispersed fluid particles [15], to more sophisticated approaches based on nucleation models [16,17].

Multiple authors [16–18] have applied the two-fluid model to perform CFD simulations of flash boiling of water in converging-diverging nozzles, using nucleation models combined with a constant bubble size or bubble number transport equation to predict the interfacial area. Generally, these authors found that the prediction of mass-flow rate and average streamwise variation of pressure and vapour volume fraction agreed well with the experimental data. Liao & Lucas [15] applied the two-fluid model to simulate flashing of water in a converging-diverging nozzle, using a constant bubble number calibrated based on the experimental data. Similar to previous studies, mass-flow rate and streamwise trends were well predicted, but a significant deviation was found in the lateral distribution of bubbles. The authors later carried out polydisperse simulations [19], but inaccuracies in the lateral distribution remained in spite of correct prediction of the bubble size spectrum. Recently, Ortego Sampedro et al. [20] proposed an interfacial area model capable of transitioning between bubbly and droplet flow regimes; it was implemented within the two-fluid model to simulate flashing of water in converging-diverging nozzles. Owing to two different values for droplet and bubble density numbers, the model turned out to be more flexible in terms of calibration and could simultaneously predict mass flow rate and efficiency of nozzles designed for flashing water. Although the majority of experimental data suitable for model validation is available for water, Zhu & Elbel [21] published experimental results on flash boiling of the refrigerant R134a in a converging-diverging nozzle with a variable-strength vortex generated at the inlet of the nozzle. In a following study [22], the authors applied the two-fluid model to simulate flashing of R134a using a nucleation model in conjunction with a bubble number density transport equation to predict the bubble size. The estimations of mass-flow rate and pressure distribution showed good agreement with the experimental data for various vortex strengths. With that being said, it should be noted that the nucleation model was calibrated based on the experimental results. In summary, despite some difficulties in predicting lateral distribution of the dispersed phase, the two-fluid model has proved capable of accurately predicting average flow properties and the phase change pattern in flashing flows.

1.2. Shape optimisation techniques for wet-to-dry expansion

Compared to the cited studies on flash boiling, modelling a wet-to-dry expansion process differs in that the expansion begins in a

two-phase state, with a vapour volume fraction greater than 0.7, and thus the dispersed phase is assumed to be in the form of droplets. The authors have previously carried out preliminary numerical assessments of wet-to-dry expansion using the homogeneous-equilibrium model [2]. However, further investigations demonstrated that non-equilibrium effects can significantly affect the phase change process and should be accounted for in numerical simulations [23]. Therefore, the authors applied the two-fluid model in a subsequent study [13] to perform two-dimensional CFD simulations of wet-to-dry expansion of the siloxane MM in a converging-diverging nozzle for a range of operating conditions and droplet sizes. Generally, the results demonstrated that wet-to-dry transition may be difficult to achieve in a nozzle with an inlet pressure below 750 kPa. On the other hand, low pressures are more attractive from the standpoint of maximising wet-to-dry cycle performance [2]. Nevertheless, the previous study did not consider any form of geometry optimisation and all the nozzles were constructed using a fixed pressure profile.

With this in mind, the optimisation of the nozzle geometry to achieve vapourisation at lower inlet pressures is attractive. Among different techniques, shape-optimisation methods, whereby a form of simulation model are coupled to an optimiser are particularly attractive. In this context, either gradient-based or gradient-free optimisation techniques can be applied to find an optimal set of design variables that maximising a defined set of objective functions. To reduce the computational cost, the optimiser is typically combined with surrogate models (metamodels), which aim at creating an approximate relationship (a so-called response surface) between the design variables and the objective functions. The response surface is constructed based on an initial database that is created using design-of-experiments (DOE) techniques, which aim to effectively resolve the design space with a minimum number of design points, which are in turn evaluated with high-fidelity methods (e.g. CFD simulations). Finally, an optimisation algorithm, such as the genetic algorithm, can be coupled with the response surface to conduct optimisation studies.

Such an optimisation framework has frequently been incorporated in the process of design and analysis of ORC turbomachinery components, where CFD solvers were often used as a means of high-fidelity evaluations. Pasquale et al. [24] performed shape optimisation of a supersonic radial turbine nozzle vane using metamodel-assisted genetic algorithm with 8–10 design variables defining the shape of the vanes. The latin hypercube was used to create the initial database, while the response surface was constructed using two different metamodels, namely the Kriging and feed-forward neural network. The optimised geometries facilitated a more gentle flow turn, resulting in a shockless expansion with more uniform flow at the stator outlet. A similar approach was followed by Persico [25], who optimised the performance of two stages of centrifugal (radial-outflow) turbine nozzles, with design variables being the control points of the B-spline defining the vanes curvature. The response surface was constructed using Kriging model based on a database created using the latin hypercube sampling. The optimisation resulted in a decrease in the total pressure loss coefficient from 4.4% to 3.1% for one of the nozzle cascades, and from 3.1% to 2.8% for the other. The optimised vanes were generally characterised by a reduced strength of a shock that appeared within the baseline geometry, facilitating a more gradual expansion. In a subsequent study [26], the authors extended the optimisation to the entire nozzle-rotor assembly, which resulted in a 2% efficiency rise of the stage. Al Jubori et al. [27] used a gradient-free optimiser to improve the performance of a small-scale ORC radial-inflow turbine by optimising the entire nozzle-rotor stage. The authors applied the optimal-space filling method to uniformly distribute the design points across the design space. Second-order polynomials were used to construct the response surface, which was coupled with a multi-objective genetic algorithm. The optimised turbine was characterised by an improved blade loading distribution, better flow guidance without flow reversal, and smaller entropy generation, which translated to an efficiency increase as high as 13.95%. Espinosa et al. [28] also used a surrogate model-based optimisation to improve the performance of an ORC radial-inflow turbine, focusing on the rotor blades, whose shape were defined by a wrap angle and two Bezier curve control points. Using a full factorial design and three-dimensional CFD simulations, a response surface was constructed based on radial basis functions. The optimiser was coupled with the genetic algorithm. The refined rotor passage resulted in a 1.9% increase in total-to-total efficiency and a 3% increase in power output. Abdeldayem et al. [29] optimised the first stage of a large-scale axial turbine operating with supercritical carbon dioxide blends. The authors used 11 design variables, defining the angle and thickness of the stator and rotor blades, and applied the central composite design as the DOE technique. A genetic algorithm coupled with a response surface created using genetic aggregation was capable of increasing the stage efficiency by 1.76 to 2.54%.

In general, the studies cited above are examples of successful incorporation of surrogate model-based optimisation techniques in the design of various turbomachinery components, which yielded significant performance improvements. In the current study, the authors attempt to carry out the first-known optimisation of a converging-diverging nozzle designed for wet-to-dry expansion. More specifically, the study focuses on the wet-to-dry expansion of siloxane MM from pressures below 650 kPa, with the aim of maximising the vapourisation rate, while maintaining an efficient expansion process. The first stage of optimisation is carried out using a previously developed nozzle design tool, which is based on a quasi-1D two-fluid model. The objective of the optimisation is to optimise the imposed pressure profile of the nozzle to maximise vaporisation rate. Since the one-dimensional code assumes inviscid flow, and as such cannot account for viscous losses, this first stage focused on maximising the vapourisation rate only. However, the optimised geometries were subsequently evaluated using two-dimensional non-equilibrium CFD simulations which served the purpose of verifying the one-dimensional optimisation, whilst providing a better understanding of the effect of nozzle geometry on the phase change process and helping to quantify the efficiency of the expansion. Within this remit, a novel approach for estimating droplet breakup within two- and three-dimensional non-equilibrium simulations of two-phase flows with phase change has been proposed and incorporated in the CFD model. In the final part of the work, multi-objective CFD-based shape optimisation of the nozzle is performed, following a surrogate model-based approach. This CFD-based shape optimisation enables the vapourisation rate and nozzle efficiency to be optimised simultaneously, which were set as the objectives of the optimisation. The results of the study provide valuable insight into the effect of the nozzle profile on the flash-boiling process, whilst providing further assessment of the feasibility of designing a wet-to-dry nozzle that could operate with low inlet pressures.

2. Two-fluid model

This section provides an overview of the two-fluid model that is employed in both the quasi-1D nozzle design tool and the CFD simulations. It also highlights the changes introduced in the model in relation to the authors' previous numerical studies; the changes aim to tailor the model to evaporating droplet flows. While this section provides an overall description of the two-fluid model, a more detailed description can be found in the previous work of the authors [13].

2.1. Model overview

The two-fluid model employs the Eulerian-Eulerian framework to simulate two-phase flows. This means that both phases are treated as interpenetrating continua, with separate mass, momentum, and energy conservation equations given as follows:

$$\frac{\partial (\alpha \rho)_\beta}{\partial t} + \nabla\left(\alpha \rho \vec{U}\right)_\beta = \dot{m}_{ex} \tag{1a}$$

$$\frac{\partial\left(\alpha\rho\vec{U}\right)_\beta}{\partial t}+\nabla\left(\alpha\rho\vec{U}\vec{U}\right)_\beta=-\alpha_\beta\nabla P+\nabla\tau_\beta+\dot{m}_{ex}\vec{U}_{ex}+M_{ex} \tag{1b}$$

$$\frac{\partial\left(\alpha\rho\, h_{tot}\right)_\beta}{\partial t}+\nabla\left(\alpha\rho\,\vec{U}h_{tot}\right)_\beta=\alpha_\beta\frac{\partial P}{\partial t}+\nabla(\alpha\lambda\nabla T)_\beta+\nabla\left(\vec{U}\tau\right)_\beta$$

$$+\dot{m}_{ex}h_{ex}+\dot{q}_{ex} \tag{1c}$$

where β is the phase index, α the volume fraction, ρ the density, $\vec{U}$ the velocity vector, P the pressure (assumed identical in both phases), τ the stress tensor, while h_{tot}, T and λ are specific total enthalpy, temperature and thermal conductivity. The volume fraction conservation equation is also solved, which states that the sum of phase volume fractions is always equal to unity. The phases interact by exchanging mass, momentum, and energy. The interphase mass exchange is denoted by $\dot{m}_{ex}$, and the products $\dot{m}_{ex}\vec{U}_{ex}$ and $\dot{m}_{ex}h_{ex}$ represent the interphase exchange of momentum and energy associated with the mass transfer. The additional momentum and energy exchange mechanisms are due to interfacial forces and heat-exchange, which are denoted as M_{ex} and $\dot{q}_{ex}$ respectively. Fig. 1 illustrates the evaporation of a liquid droplet with a diameter D_d during wet-to-dry expansion. Because of finite rates of momentum and heat transfer, the liquid and vapour can have different temperatures (T_L and T_V), and velocities (u_L and u_V). The mass transfer is determined using a two-resistance model, which assumes that both phases exchange heat with an interface that is at local saturation temperature T_{sat} (the effect of pressure non-equilibrium is neglected). Assuming that the liquid-vapour interface has no capability to store heat, an energy balance can be applied at the interface to determine the interphase mass exchange rate:

$$\dot{m}_{ex}=\frac{\dot{q}_{ex}}{h_L-h_V}=\frac{\mathfrak{H}_L A_{int}\left(T_{sat}-T_L\right)+\mathfrak{H}_V A_{int}\left(T_{sat}-T_V\right)}{h_V-h_L} \tag{2}$$

where $\dot{q}_{ex}$ is the heat exchange across the interface, equal to the sum of $\dot{q}_L$ and $\dot{q}_V$, A_{int} is the interfacial area concentration per unit volume, $\mathfrak{H}$ is the heat-transfer coefficient, while h is the specific enthalpy; the subscripts L and V denote the liquid and vapour phases respectively. The interfacial area is the total surface area of the droplets per unit volume, which for spherical droplets can be expressed as:

$$A_{int}=N_d\,\pi D_d^2=6\frac{\alpha_L}{D_d} \tag{3}$$

where N_d is the number of droplets per unit volume (droplet number density), and D_d is the droplet diameter. Therefore, to determine the mass and heat exchange, one must know the liquid and vapour heat transfer coefficients, as well as the droplet diameter. When it comes to the momentum exchange, the primary interfacial force acting in the direction of the flow is the drag force. Secondary interfacial forces relevant to droplet flows include lift and turbulent dispersion forces. The first acts in the direction perpendicular to the flow and is responsible for lateral migration of droplets, while the latter accounts for the interaction between the turbulent vapour eddies and the dispersed droplets; it enhances mixing of the two phases, distributing the droplets from areas of high concentration to areas of low concentration.

2.2. Interphase models

In order to estimate the heat-transfer coefficients, and the three coefficients defining the interfacial forces, one can resort to the open literature, which contains a range of correlations, typically derived empirically. These correlations are often referred to as interphase models and can significantly influence the solution. Therefore, it should be ensured that the selected model is suitable for the investigated problem. With this in mind, the authors have previously carried out sensitivity studies to evaluate the effect of different interphase models on the wet-to-dry expansion process [13]. Generally, the qualitative flow behaviour was similar when different interphase models applied, however there were some quantitative discrepancies with regards to heat-transfer coefficients, especially for that on the liquid side. On the other hand, the interphase models used for the momentum transfer had very little effect on the solution. This section explains the selection of the interphase models, highlighting any introduced changes in relation to previous wet-to-dry expansion studies.

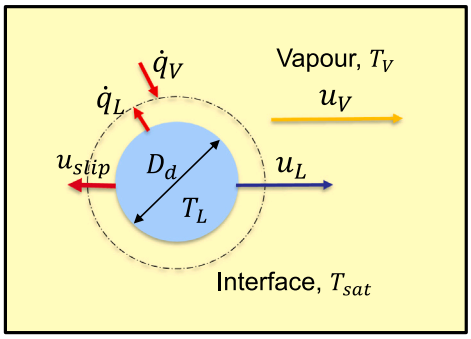

Fig. 1. Schematic drawing of an evaporating droplet in the wet-to-dry expansion.

The heat-transfer coefficient on the continuous vapour side is evaluated with the Ranz-Marshall [30] correlation, derived from experimental tests on a water droplet evaporating in a hot air stream. It is more challenging to estimate the heat-transfer coefficient between the droplet and the interface. In previous studies, the authors assumed a constant Nusselt number of 6, which comes from heat-transfer analysis in a solid sphere. Nevertheless, the heat transfer will likely be enhanced in a droplet due to effects such as internal circulation. To more accurately predict the heat transfer rate, a correlation applied in RELAP5/MOD3 [31], a code designed for transient simulation of flashing in light water reactor coolant systems, was adapted in this work. The correlation is based on Brown's [32] work on condensation of water droplets:

$$Nu_L=2+7\min\left(1+\frac{c_{p,L}\,\max(0,\,|T_{sat}-T_L|)}{h_{LV}},8\right) \tag{4}$$

where Nu_L is the liquid Nusselt number, $c_{p,L}$ is the liquid specific heat capacity at constant pressure, h_{LV} is the latent heat of vapourisation. This correlation was originally obtained for droplets suspended in a hotter medium. However, the authors assume that similar heat-transfer coefficients can be expected for droplet cooling, and the correlation serves as the current best-estimate. As for the momentum exchange, the three interfacial forces relevant to droplet flows are drag, lift and turbulent dispersion forces. The drag coefficient was estimated using the Ishii–Zuber [33] correlation, which was also used in previous simulations. The correlation is applicable to droplet flows with either dilute or densely distributed droplets. The formulations used for the lift and turbulent dispersion forces have been updated in the current work. To evaluate the lift force, the Legendre & Magnaude [34] was applied, which is more suited to small fluid particles. The previously applied turbulent dispersion model was more suitable for bubbly flow; since liquid droplets are significantly denser than vapour, they are not so easily caught in vapour turbulent eddies. This was accounted for by setting a turbulent dispersion coefficient that depends on the turbulent Stokes number: $c_{TD}=e^{-0.5St_t}$, where c_{TD} is the dispersion coefficient, while St_t is the turbulent Stokes number. In case the droplet relaxation time is much higher than the turbulent eddy lifetime, the droplets will be weakly affected by the eddies. Hence, the turbulent dispersion tends to zero as the turbulent Stokes number increases.

The most significant parameter affecting the wet-to-dry expansion is the droplet size, which is difficult to estimate without resorting to experimental data. Previous numerical studies on wet-to-dry expansion considered a range of different droplet density numbers to investigate the overall effect of droplet size on the expansion. Unlike flashing from a subcooled or saturated liquid state, wet-to-dry expansion begins from two-phase conditions, and the nucleation models cannot be directly

used to estimate population and size of the dispersed fluid particles. Having said that, the expansion in the wet-to-dry nozzle is characterised by a rapid flow acceleration to supersonic velocities. Under such conditions, large droplets are likely to break up into smaller fragments due to high velocity gradients associated with large drag forces. In this way, the local flow conditions can be related to the maximum stable droplet size, which was done in this work by resorting to the definition of Weber number. The Weber number is a dimensionless parameter frequently used in atomisation studies. It relates the aerodynamic forces acting to fragment the droplet to the surface tension that resists that fragmentation:

$$We = \frac{\rho_V D_d \left|u_V - u_L\right|^2}{\sigma} \tag{5}$$

where We is the Weber number and σ is the surface tension coefficient. Experimental results indicate that as long as:

$$\frac{\mu_L}{\rho_L D_d \sigma} < 0.1 \tag{6}$$

which is satisfied in all the investigated cases, droplet breakup in both subsonic and supersonic flow regimes is expected to initiate when We > 11 [35,36]. Hence, assuming no coalescence, the droplet variation in the nozzle can be estimated. It should be emphasised that the physical droplet breakup process is complicated, and the droplet breakup model described here does not aim at resolving the process but rather uses the critical Weber number to estimate a realistic droplet size under given flow conditions. It was also found useful in the optimisation studies, as it allowed to relate the shape of the nozzle, which defines the rate of expansion, to the resulting droplet size.

The two-fluid non-equilibrium model used in this work has been previously validated to an extent in the previous work of the authors [13]. The experimental data used for the validation was taken for flash boiling studies of subcooled/saturated water [5]. Having said this, it is important to highlight that the physics of the wet-to-dry expansion studied in this current work differs from the flash boiling experimental tests conducted in the past. The wet-to-dry expansion begins with a partially evaporated fluid with vapour volume fraction close to 90%. As such, the expansion does not involve bubble nucleation process, and the dispersed phase is in the form of liquid droplets. In the same vein, since it is still a flashing process, the physics of wet-to-dry expansion also differ from studies concerning condensation in steam turbines, where modelling droplet nucleation is of primary importance. Hence, there is no experimental data available to validate the CFD model specifically for wet-to-dry expansion. Therefore, the model set up for the validation had to eventually be adjusted for flashing droplet flows. Additional sensitivity studies related to the employed interphase models were performed to help ensure the model is reliable. However, the authors acknowledge uncertainty remains due to the lack of directly relevant experimental data.

3. Numerical implementation

This section describes how the two-fluid model described in the previous section was implemented in the quasi-1D nozzle design tool and in the non-equilibrium CFD simulations, followed by results from the mesh independence study.

3.1. Quasi-1D nozzle design tool

In the previous work, the authors developed a quasi-1D non-equilibrium design tool to design nozzles for wet-to-dry expansion [23]. The design tool is based on a simplified formulation of the two-fluid model described in Section 2. The flow is assumed to be steady, quasi-1D and inviscid, varying only in the longitudinal direction. Consequently, lift and turbulent dispersion forces are not included, and the governing equations given by Eqs. (1a)–(1c) are reduced to:

$$\frac{1}{A}\frac{\partial\left(\alpha\,\rho\right)_\beta}{\partial x} = \dot{m}_{ex} \tag{7a}$$

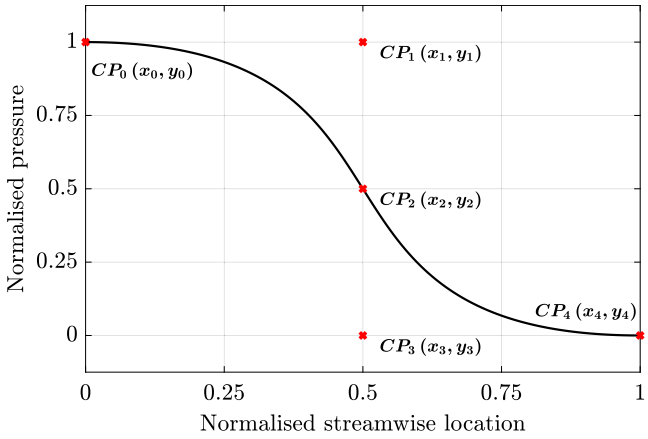

Fig. 2. Normalised baseline nozzle pressure profile constructed using a Bezier curve with five control points; the red asterisks (*) show the location of the Bezier curve control points.

$$\frac{1}{A}\frac{\partial\left(\alpha\,\rho A u^2\right)_\beta}{\partial x} = -\alpha_\beta\frac{\partial p}{\partial x} + F_D \tag{7b}$$

$$\frac{1}{A}\frac{\partial\left(\alpha\,\rho A u h_{tot}\right)_\beta}{\partial x} = \dot{m}_{ex}h_{ex} + \dot{q}_{ex} \tag{7c}$$

where A is the nozzle cross sectional and F_D is the interfacial drag force. The nozzle design routine is initiated with the selection of the working fluid and boundary conditions, which include inlet pressure, vapour quality and mixture velocity. Since the nozzle is studied in the context of turbomachinery, and intended as a stator of a turbine integrated within the wet-to-dry cycle, the cycle condensation temperature and the turbine degree of reaction are used to define the nozzle outlet pressure. This is also the reason why the investigated nozzles are planar converging-diverging nozzles of a rectangular cross-section. The quasi-1D tool follows an inverse design approach, where the Eqs. (7a)–(7c) are solved to converge on an imposed pressure profile, which is controlled using a 4th order Bezier curve with five control points (Fig. 2). The equations describing the Bezier curve are given as:

$$x(t) = (1-t)^4x_0 + 4(1-t)^3tx_1 + 6(1-t)^2t^2x_2 + 4(1-t)t^3x_3 + t^4x_4 \tag{8a}$$

$$y(t) = (1-t)^4y_0 + 4(1-t)^3ty_1 + 6(1-t)^2t^2y_2 + 4(1-t)t^3y_3 + t^4y_4 \tag{8b}$$

where t is a parameter variable varying between 0 and 1, while x_n and y_n are the normalised streamwise and pressure. The x and y coordinates, denoted x_0 through to x_4 and y_0 through to y_4, represent the position of the five control points on the non-dimensional plane. The first and last control points are fixed with (x_0, y_0) and (x_4, y_4) at $(0, 1)$ and $(1, 0)$ to ensure that the pressure is equal to the design inlet and outlet values at the nozzle entrance and exit respectively. Furthermore, the vertical position of CP_1 and CP_3 are fixed at $y_1 = 1$ and $y_3 = 0$ to ensure that the pressure gradient approaches zero at the inlet and outlet of the nozzle. In summary the shape of the pressure profile is determined by the position of the four free coordinates: x_1, x_2, y_2 and x_3.

An exemplary pressure profile is illustrated in Fig. 2. This is identical to the profile used in all previous investigations and will be referred to as the baseline profile in this work. In this profile, all three movable control points, CP_1, CP_2 and CP_3 are positioned at $x_n = 0.5$, while the pressure at the middle of the nozzle is set to the average of the inlet and outlet pressures ($y_2 = 0.5$). Previous CFD studies indicate that such a pressure distribution results in a gradual shock-free expansion [13]. Having defined the pressure distribution, the governing equations (Eqs. (7a)–(7c)) were discretised with a second-order accurate backward scheme, and solved to satisfy the imposed profile. The fluid properties, including metastable liquid and vapour properties, were evaluated using NIST REFPROP 10.0 [37]. To fully define the nozzle geometry,

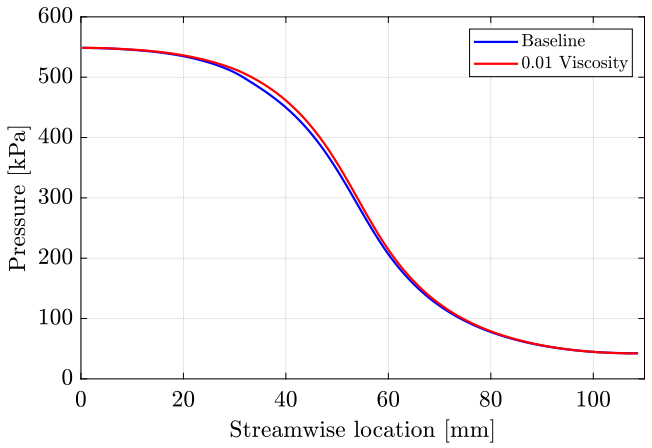

Fig. 3. The effect of viscosity on average streamwise pressure distribution within the wet-to-dry nozzle.

the ratios of nozzle length to throat height (L/o_{th}), and nozzle width to throat height (b/o_{th}) are set as model inputs.

It is worth noting that the nozzle design tool assumes inviscid flow. However, previous studies have demonstrated the significance of viscous losses in flash boiling phenomena, and in particular the influence of viscous losses on the nozzle pressure distribution [12]. However, these studies have typically dealt with the expansion from a subcooled or saturated liquid state, where a substantial portion of the expansion occurs with a high liquid volume fraction. On the contrary, in the current work the two-phase expansion begins with liquid volume fraction close to 10%, which further diminishes downstream. Therefore, the channel is mostly occupied by the less viscous vapour phase throughout the expansion, which is why viscous losses are expected to be less significant than in pure liquid flashing processes. To verify this assumption, one of the simulations reported later was run with the viscosity of both phases reduced by a factor of 100. The average streamwise pressure distribution shown in Fig. 3 demonstrates a rather negligible effect of viscosity on the pressure distribution within the wet-to-dry nozzle. The comparison of mass-flow rates also showed negligible impact (<0.01%).

3.2. Computational-fluid dynamics setup

To carry out the CFD simulations, the two-fluid model was implemented in ANSYS CFX 2021 R1 [38] to carry out steady-state quasi-two-dimensional simulations. The solver follows the finite-volume approach to solve the Reynolds-averaged Navier–Stokes (RANS) equations. The analysed nozzle is a planar converging-diverging nozzle with a rectangular cross-section. Although CFX only allows for three-dimensional simulations, a thin nozzle slab with a thickness of 0.15 mm was imported to ANSYS, applying a symmetric boundary condition to the upper and lower faces of the slab to perform quasi-2D simulations. In contrast to the nozzle design tool, the CFD results give insight into the effect of both longitudinal as well as lateral flow variations. Moreover, the viscosity and turbulence effects were included alongside the lift and turbulent dispersion forces, which could not be accounted for in the quasi-1D code. Second-order accurate schemes were applied to discretise the advection and turbulence equations. Turbulence in the continuous phase (vapour) was modelled using the $k-\omega$ SST model, while a dispersed zero equation model was used to estimate the eddy viscosity in the dispersed phase [39]. CFX uses an automatic wall function method, which automatically switches from directly resolving the boundary layer to standard wall functions depending on the local y^+ value. To evaluate the thermodynamic and transport properties of the working fluid, look-up tables were coupled with the CFD solver.

Table 1
The summary of two-phase flow model setup in the nozzle design tool and CFD solver.

	CFD	Nozzle design tool
Simulation type	2D steady viscous	1D steady inviscid
Multiphase flow model	Two-fluid model	Two-fluid model
Turbulence	$k-\omega$ SST	n/a
Heat transfer	Liquid: Brown [32] Vapour: Ranz–Marshall [30]	Liquid: Brown [32] Vapour: Ranz–Marshall [30]
Drag	Ishii–Zuber [33]	Ishii–Zuber [33]
Lift	Tomiyama [40]	n/a
Turbulent dispersion	Favre averaged drag	n/a

The look-up tables were generated using NIST REFPROP 10.0, which uses an equation of state based on Helmholtz energy derived from empirical data and molecular simulation data for siloxane MM [37]. The liquid and vapour properties were extended into the metastable region and calculated up until the spinodal limit so that the solver could evaluate phase properties when the liquid and vapour phases became superheated and subcooled respectively. Table 1 summarises the setup of the two-phase flow model the nozzle design tool and the CFD solver.

3.2.1. Modelling breakup in the CFD solver

In this work, it is assumed that liquid droplets can change size only due to breakup, while coalescence effects are neglected. This means that the droplet diameter could either remain constant if the Weber number stays below the critical value or decrease in the streamwise direction if it exceeds the critical value. Therefore, computational modelling of breakup requires not only the knowledge of flow conditions at a given streamwise position but also the knowledge of droplet size upstream of that position to ensure that the droplet diameter does not begin increasing in the streamwise direction. This can be fairly easily implemented in one-dimensional codes since the equations are typically solved by marching along the longitudinal axis of the nozzle [23,41]. On the other hand, approximating the breakup process in such a manner in two- or three-dimensional CFD simulations is less straight forward and to the best of the authors' knowledge, it has not yet been attempted. Therefore, in the current study, a novel approach to approximating the breakup process in two- and three-dimensional two-phase flows is introduced by discretising the nozzle into a number of control volumes along the nozzle's longitudinal axis, as shown in Fig. 4. In this way at a single iteration within the simulation it is possible to simultaneously estimate the critical diameter in each control volume based on the average flow conditions and implement a simple expression that prevents the droplets from increasing in size in the streamwise direction. Alongside this, an initial droplet diameter at the inlet to the nozzle is specified, which is set to 0.1 mm. The shortcoming of such an approach is that the averaged droplet diameter varies only along the longitudinal axis of the nozzle, and thus no lateral variations are considered. It should also be pointed out that even though this study refers to this droplet size estimation routine as a breakup model, the physical breakup is a much more complicated process. As such, the model herein described should be considered as a simplified technique of estimating maximum stable droplet size under given flow conditions.

In theory, the nozzle could be divided into a very high number of volumes to make sure that the droplet breakup process is well resolved. However, it was found that a high number of volumes was associated with significantly longer simulation times, which is thought to be related to the additional burden of calculating average properties within each volume. In the context of shape optimisation, which may involve a large number of simulations, it is desired to reduce the simulation time as much as possible. Therefore, calibration studies were conducted to determine where the breakup is most likely to occur and to limit the discretisation to that location. Since the breakup is closely linked to the shape of the nozzle, two different geometries were tested, which represent two extremes corresponding to very gradual

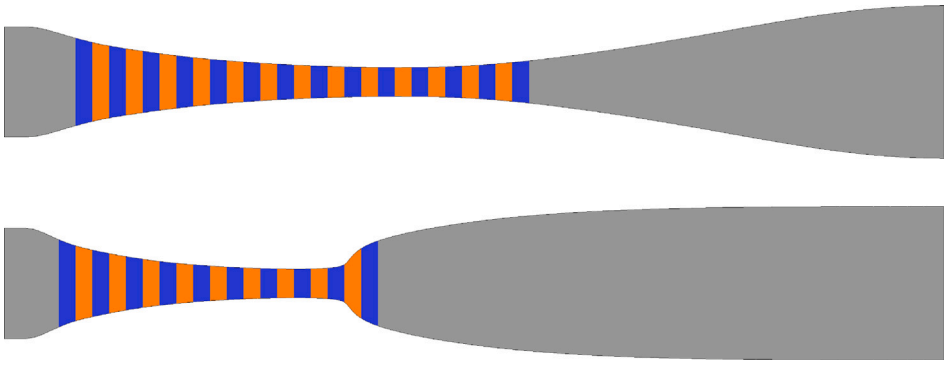

Fig. 4. The breakup zone in the baseline (top) and 1D-optimised (bottom) nozzles expanding the two-phase mixture from 550 kPa and inlet quality of 0.3; the blue and orange stripes represent the control volumes used to approximate the breakup, which signify the location of breakup.

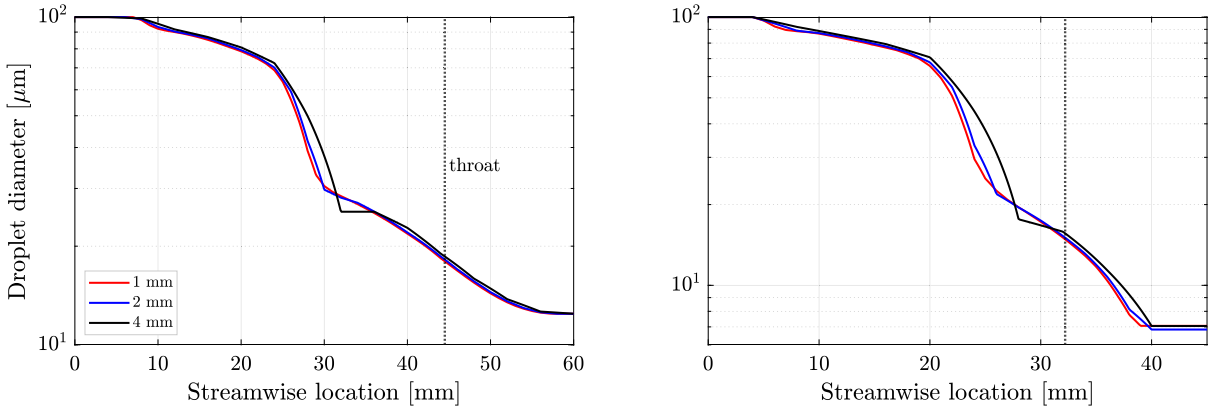

Fig. 5. The relationship between the width of the volumes used to model the breakup and the streamwise variation of the average droplet diameter; the two plots correspond to the baseline (left) and 1D-optimised (right) nozzles expanding the two-phase mixture from 550 kPa and inlet quality of 0.3.

and abrupt expansions. The first geometry was the baseline nozzle with a pressure profile illustrated in Fig. 2, while the latter was a geometry obtained from one-dimensional optimisation described in the following sections. The length of the two nozzles was identical and equal to 109.39 mm, while the throat location differed, being at 44.5 and 32.2 mm from the inlet in the baseline and optimised nozzles respectively. An identical expansion from 550 kPa and inlet quality of 0.3 was simulated, and an appropriate mesh size was selected in accordance with the mesh independence study described in the next subsection. The goal of these calibration studies was to find the region where breakup occurs, as well as to determine a suitable width of the control volumes needed to accurately capture the breakup process. The results in Fig. 4 illustrate the location of the breakup as predicted by the CFD simulations for the two investigated geometries. The breakup was found to begin very close to the inlet in both nozzles; however, in the case of the gradual expansion, the breakup process extended over larger length of the nozzle. More specifically, the breakup ceased at a distance of around 15 mm downstream of the throat in the baseline nozzle, compared to around 10 mm for the optimised nozzle. It was thus decided to place the control volumes between the nozzle inlet and 16 mm downstream of the throat, which should capture the breakup in both gradual and abrupt-expansion nozzles. The second part of the sensitivity analysis concerned the width of the volumes required for accurate prediction of the droplet diameter profiles. To this end, the breakup zones shown in Fig. 4 were discretised with volumes of a width ranging from 1 to 4 mm. The results in Fig. 5 illustrate the relationship between the width of the volume and the streamwise variation of the average droplet diameter. It can be noted that the droplet diameter profiles are very similar for the width of 1 and 2 mm. Therefore, the width of 2 mm was considered to be sufficiently small for approximating the breakup process.

3.2.2. Mesh independence study

The mesh independence study was conducted on the 1D-optimised nozzle shown in Fig. 4. Three different grids were constructed: a coarse mesh with approximately 7,500 elements, a moderate mesh with 15,000 elements and a fine mesh with 30,000 elements. Compared to the authors' previous studies, the grid was improved by constructing a fully structured hexahedral mesh, eliminating low-quality distorted elements. The resolution of the mesh was refined near the wall and in the proximity of the nozzle throat. The width of the element adjacent to the wall was kept constant at 10 μm in each grid. It was found that reducing the width below 10 μm caused solution convergence issues, which is not completely understood by the authors since the mesh quality remained high. With that being said, the width of 10 μm was sufficient for the average y^+ of vapour and liquid to remain below 50 and 150 respectively, where standard wall functions could be applied. Because of the nature of the studied flow, the behaviour of the two-phase mixture in the boundary layer may deviate from the standard wall laws developed for canonical flows. However, the two-fluid model applied in this study simplifies the problem by treating the two-phase flow as composed of two interpenetrating continua with the velocity profile estimated for each phase separately, similar to single-phase flows. The difference lies in the addition of interfacial forces that affect the velocity of both phases. As such, even though in reality the mixture could exhibit more complex behaviour, in the context of the employed modelling framework, it seems reasonable to assume that the standard wall functions are applicable. Furthermore, the preliminary assessment of viscosity effects (see Fig. 3) indicates that these effects are not critically important in the wet-to-dry expansion due to low volume fraction of the more viscous liquid phase. The width of the elements applied in the lateral direction was progressively smaller when approaching the nozzle wall, to ensure that the boundary layer is well resolved.

Table 2
Mesh independence study results.

Mesh	Coarse	Moderate	Fine
Element count	7520	15 066	29 988
Longitudinal elements	188	243	357
Lateral elements	40	62	84
$q_{V,out}$ [%]	93.31	93.43	93.39
$u_{V,out}$ [m/s]	233.25	234.06	234.31
$u_{L,out}$ [m/s]	215.00	216.67	216.75
$T_{V,out}$ [°C]	99.70	99.85	100.02
$T_{L,out}$ [°C]	76.29	76.13	76.33
$\dot{m}_{out}$ [g/s]	1.715	1.708	1.708
η_N [%]	74.12	74.69	74.84
Δ_{max} [%]	–	0.77	0.20

Based on simplified estimations of the boundary layer thickness, it was estimated that the boundary layer was resolved with approximately 20 elements. The convergence of the solution was assessed based on the average residual values along with the solution mass imbalance, and various flow parameters such as mass flow rate, and averaged velocities and vapour mass fractions taken at several planes along the nozzle. Moreover, several monitor points were placed in the diverging and converging sections, and at the throat to additionally examine the convergence. The solution converged well within several thousand of iterations, with the average mass and momentum residuals below 10^{-6}, mass imbalance less than 0.005% and various averaged and local flow parameters converging to single values.

The results of the mesh independence study are summarised in Table 2, including information on mesh metrics, various outlet flow properties, nozzle efficiency (η_N) and total mass-flow rate at the outlet ($\dot{m}_{out}$). The nozzle efficiency is calculated based on the ratio of the actual to isentropic kinetic energy rise:

$$\eta_N = \frac{\left(\dot{m}_{V,out}u_{V,out}^2 + \dot{m}_{L,out}u_{L,out}^2\right) - \dot{m}_{in}u_{in}^2}{\dot{m}_{out}u_{is,out}^2 - \dot{m}_{in}u_{in}^2} \tag{9}$$

where $\dot{m}_{in}$ is the total mass-flow rate at the inlet, while $u_{is,out}$ is the isentropic outlet velocity, which is estimated with a simple code based on a quasi-1D isentropic homogeneous-equilibrium expansion. Since the study is concerned with non-equilibrium two-phase flows, where liquid and vapour may significantly deviate from thermodynamic equilibrium, the vapour mass fraction, q_V, was defined as the ratio of the vapour mass-flow rate to the total mass-flow rate:

$$q_V = \frac{\dot{m}_V}{\dot{m}_V + \dot{m}_L} \tag{10}$$

Based on the mesh-independence study results reported in Table 2, a percentage variation in each reported parameter between two consecutive grids, i.e. between the moderate and coarse, and between the fine and moderate grids, was calculated. The maximum of these percentage variations, Δ_{max}, is reported at the bottom of the table. The greatest difference between the moderate and coarse grid was below 0.77%, and it corresponded to the outlet velocities and nozzle efficiency. The maximum difference dropped to around 0.20% between the fine and moderate grids. Generally, all the grids generated very similar results when it comes to the outlet flow properties, with the difference becoming practically negligible when the number of elements was greater than 15,000.

Alongside the outlet properties, average streamwise variations were also examined, which were calculated using a custom user-defined script. The averaging routine relied on defining a number of cross-sectional planes stretching between the inlet and outlet of the nozzle and calculating the average of a phase-dependent property, ϕ, with the following expression:

$$\phi_{avg} = \frac{\int \left(d\dot{m}_L\phi_L + d\dot{m}_V\phi_V\right)}{\dot{m}_L + \dot{m}_V} \tag{11}$$

where the summation is carried out over all mesh elements across the cross-sectional plane. Several average streamwise variations were examined but no significant deviations were found except for the mass-flow averaged entropy profiles, which are plotted in Fig. 6.

It is observed that the averaged entropy differs for the coarse mesh from the very beginning of the expansion, despite that overall trend and entropy generation being almost identical (Fig. 6 (right)). The vapour and liquid entropy values at the inlet were found to be identical and the difference was found to be related to a slightly different ratio of vapour and liquid mass-flow rates, which were used in the averaging. The percentage difference in average streamwise entropy profiles between the moderate and coarse grids oscillates in the 0.25–0.35% range, which drops to around 0.10–0.15% for the fine mesh. Based on the mesh independence study results it was decided that the mesh with 30,000 elements was sufficiently fine.

4. One-dimensional optimisation

The nozzle design tool used in this study relies on imposing the pressure profile which is constructed with a Bezier curve (see Fig. 2). The pressure profile influences the rate of the expansion, which in turn affects the breakup process and the resulting droplet size. Since the droplet size is arguably the most important factor influencing the rate of mass and heat transfer [13], the optimisation of the pressure profile imposed in the design of the nozzle could help maximise the vapour outlet quality. The design process assumes a quasi-1D non-equilibrium flow as discussed in Section 3.1. As such the optimisation of the pressure profile will be referred to as one-dimensional optimisation. This section first explains what operating conditions were considered for the optimisation, followed by the verification of the quasi-1D nozzle design tool with CFD simulations. The one-dimensional optimisation setup and results are then presented and discussed.

4.1. Investigated operating points

Previous cycle studies focused on optimisation of the wet-to-dry cycle indicate that siloxane MM is a promising candidate for the wet-to-dry cycle, being capable of providing relatively high thermodynamic advantage over single-phase cycles, while mitigating certain technical challenges such as extremely high expansion ratios or near-vacuum condensation [2]. The cycle studies have also revealed that two-phase expansion gives the greatest advantage when the heat source is at temperature between 150 and 200 °C, where the power output could be between 29% and 14% higher when compared to a simple ORC. This temperature range corresponds to an evaporation pressure in the range of approximately 300 kPa to 1000 kPa, if the siloxane MM is used. With that being said, previous numerical studies also indicate that a complete wet-to-dry transition may be difficult to achieve when expanding from pressures lower than 750 kPa and from vapour qualities below 30% [13]. For this reason, the optimisation was applied to three operating points with low inlet pressures, namely, 450, 550 and 650 kPa. These pressure levels could correspond to heat source inlet temperatures in the approximate range of 170 to 190 °C, where the cycle can potentially offer a significant power output increase [2]. Inlet vapour quality was set to 0.3, which provides the good balance between the cycle thermodynamic advantage while enabling wet-to-dry transition. The nozzle was designed as if it was a part of a turbine designed for the wet-to-dry cycle. Hence, the degree of reaction and cycle condensation temperature were applied to calculate the nozzle outlet pressure. In this work, these two parameters were set to 0.4 and 40 °C respectively, which gave the outlet pressure of 39.77, 43.78 and 47.32 kPa for the expansions with inlet pressure at 450, 550 and 650 kPa respectively.

The three expansion cases are reported in Fig. 7, which shows the ideal isentropic process. Although expanding from lower inlet qualities could offer a further increase in the power output, preliminary turbine

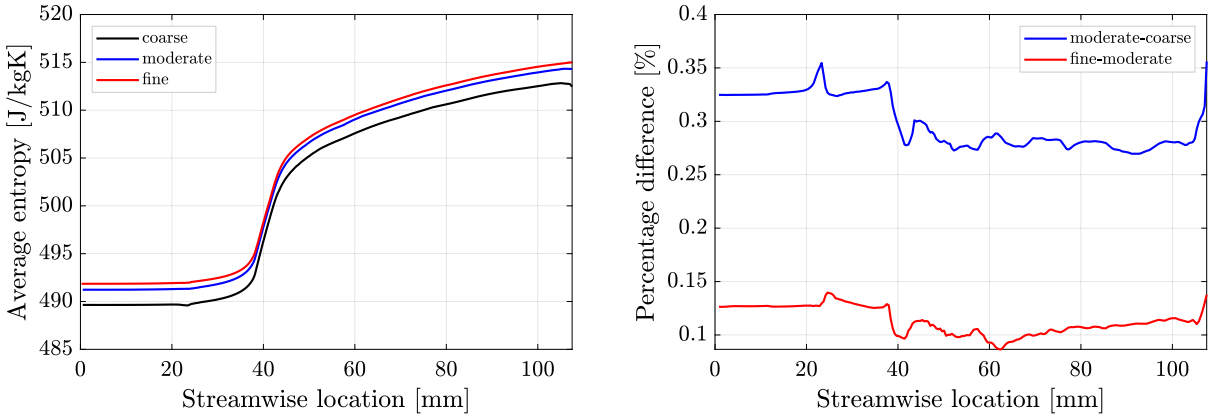

Fig. 6. Streamwise variation of mass flow-averaged entropy for various grid sizes (left) and percentage difference in average entropy between the consecutive grids (right).

Table 3
Geometrical features of each investigated converging-diverging nozzle.

P_{in} [kPa]	$q_{V,in}$	P_{out} [kPa]	H_{in} [mm]	o_{th} [mm]	H_{out} [mm]	L_{th} [mm]	L_N [mm]
450	0.30	39.77	14.56	3.74	18.78	49.09	119.49
550	0.30	43.78	13.14	3.43	18.20	44.50	109.39
650	0.30	47.32	12.04	3.21	17.74	40.75	101.66

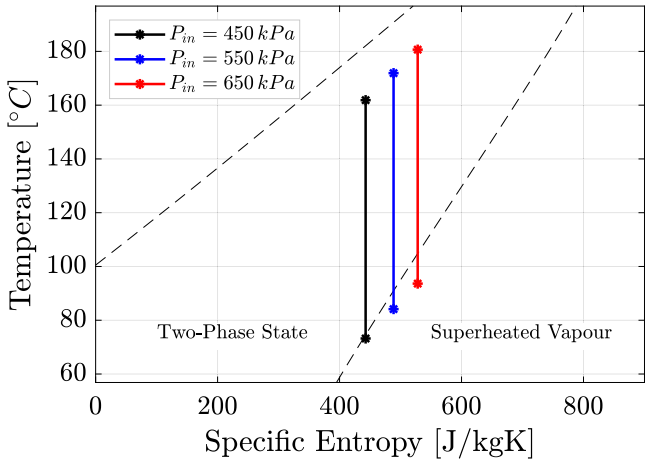

Fig. 7. Three operating points investigated in the optimisation study; the expansions shown under the isentropic flow assumption.

design studies have shown that it would require a lower degree of reaction, which could have a detrimental effect on the turbine efficiency [2]. The mass-flow rate was set to 0.12 kg/s, which translates to a turbine isentropic power of around 100 to 120 kW under the investigated operating conditions. This power output is estimated assuming that the turbine has sixteen stator vanes; each nozzle representing one stator vane. This power rating could correspond to a small-scale system designed for waste-heat recovery from low-temperature sources. It is worth mentioning that the authors previously compared the results for different power scales, and found that the scale of application did not significantly affect the vapourisation rate and the overall phase change process. Finally, the ratios of nozzle length to throat height (L/o_{th}), and nozzle width to throat height (b/o_{th}) were set to 30 and 3 respectively, which are values in line with former studies. Based on a preliminary assessment of the effect of various geometrical parameters on the wet-to-dry expansion, it was found that neither the length or the height of the passage significantly affects the vapourisation rate. However, the nozzle efficiency was found to be more sensitive to the passage width and length and could vary by several percent.

Fig. 8 illustrates the baseline nozzle geometry for the expansion from 550 kPa. The baseline nozzles for the two other investigated cases (with P_{in} at 450 and 650 kPa) had similar shapes. Using the same notation defined in Fig. 8, Table 3 provides the dimensions of all the investigated nozzles. It is worth noting that even though the baseline nozzles will undergo optimisation, all the parameters except for the streamwise location of the throat (L_{th}) will remain unchanged. This is because the design inlet and outlet conditions as well as the design mass-flow rate, which determines the throat height (o_{th}) are held constant.

4.2. Comparison of nozzle design tool against CFD simulations

Before proceeding with the optimisation, the performance of baseline nozzles generated using the quasi-1D tool has been verified using the CFD model. Although preliminary comparisons have already been performed by the authors in a previous study [42], several modifications have since been made. Firstly, as highlighted in Section 2.2 the liquid side heat-transfer coefficient, alongside the lift and turbulent dispersion forces, used in the CFD model have been updated. The drag force equation was also corrected in the quasi-1D tool, which previously caused a discrepancy in the velocity slip. Alongside this in the CFD simulations the vapour thermodynamic quality was previously used to measure the evaporation rate. However, in the presence of significant non-equilibrium effects, it is more appropriate to use the vapour mass fraction calculated based on the ratio of mass-flow rates, as defined in Eq. (10). Finally, the droplet breakup modelling described in Section 3.2.1 has been implemented. The three nozzles for the operating points defined in Fig. 7 were designed using the baseline pressure profile shown in Fig. 2. These were assessed using the quasi-2D steady-state CFD simulations, as described in Section 3.2.

Fig. 9 presents the comparison of the average streamwise pressure variations between the quasi-1D design tool and the CFD model. The results indicate that the pressure distribution slightly diverged from the design profiles within the diverging section of the nozzle. A close-up of the profiles near the nozzle outlet reveals a slight overexpansion for the 550 and 650 kPa cases. However, this is rather insignificant, with the outlet pressure being approximately 2.5% lower than the design value. This effect was slightly more pronounced for the 450 kPa case, with flow reaching a pressure 7.6% lower than the design pressure. Overall, the pressure profiles estimated with CFD were relatively close

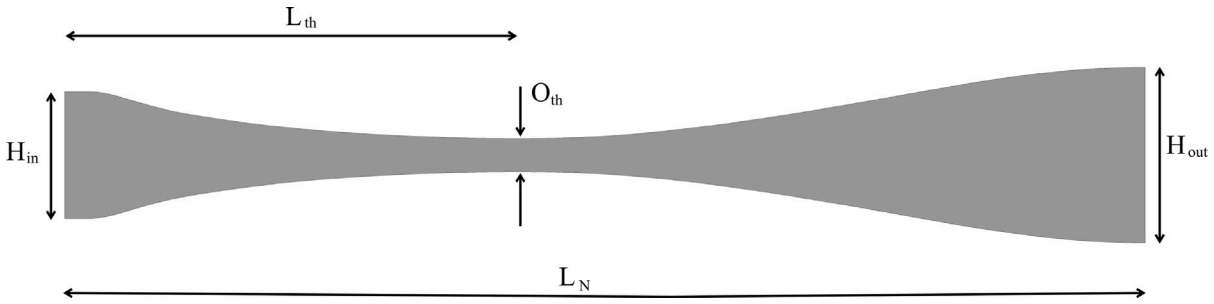

Fig. 8. Baseline nozzle geometry for the expansion from 550 kPa.

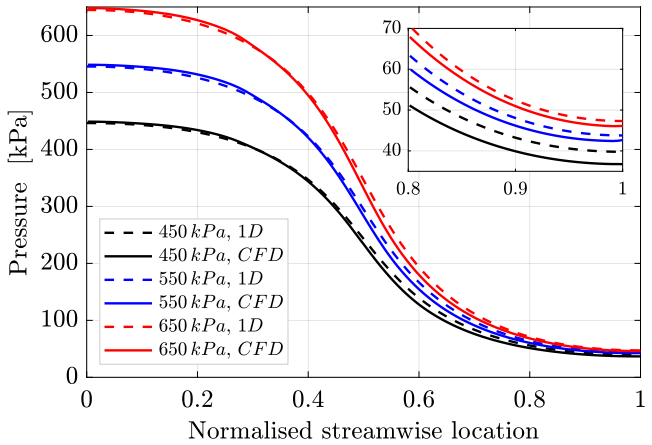

Fig. 9. Comparison of average streamwise variation of pressure between the quasi-1D design tool and CFD; the box in the top right presents a close-up of the variations near the nozzle outlet.

to the design ones. The results shown in Fig. 10 compare the average streamwise variation of vapour quality (x_V) and velocity slip for the different nozzles. The quasi-1D tool predicts near-dry conditions at the nozzle outlet with x_V ranging from 0.984 to 0.998. Most of the phase change occurs shortly past the throat in the diverging section. The curve then flattens as the flow approaches the outlet. This trend is similar for each of the three expansions; however, the higher the pressure the quicker the evaporation and the higher the outlet vapour quality. Although the CFD model predicts a visibly lower evaporation rate compared to the quasi-1D design tool, the phase-change pattern looks very similar in both cases. The discrepancy in x_V gradually increases in the diverging section, reaching a maximum of around 10 to 15% at the outlet. In summary, the lateral phase separation, viscosity, and turbulence effects are likely to delay the evaporation and lead to increased liquid content in the flow leaving the nozzle. Among these effects, the lateral phase separation is considered to have the greatest impact on the phase change process. This is because as the phases separate out there are areas of highly-concentrated liquid, characterised by reduced interfacial area available for the heat transfer, which drives the mass exchange according to Eq. (2). Owing to the corrected drag equation, there is a much better agreement between the velocity slip profiles, compared to authors' previous verification study [42]. Overall, the slip predicted by the quasi-1D tool is much higher, which translates to a smaller droplet size in the nozzle diverging section due to enhanced droplet breakup (see Eq. (5)), and consequently higher evaporation rates due to increased ratio of liquid volume to the interfacial area. It is worth noting at this point that the maximum velocity slip reaches 40 m/s; knowing that the mixture velocity at this point is the range of 230 to 250 m/s, the corresponding slip velocity is between 14 and 17% of the mean mixture velocity. Therefore, the assumption of homogeneous flow in case of wet-to-dry expansion may be invalid. Despite the quantitative differences between the quasi-1D design tool and the CFD, the overall phase change pattern is conserved. Therefore, it seems rational to assume that enhancing the evaporation rate in the quasi-1D tool will translate to enhanced evaporation in the CFD. This justifies using the quasi-1D tool for initial optimisation purposes.

4.3. One-dimensional optimisation results

As apparent from Fig. 10, achieving complete mixture evaporation at pressures below 650 kPa is challenging. This study aims to enhance evaporation by optimising the nozzle pressure distribution to assess whether complete evaporation could be achieved in low-pressure expansions. A non-linear constrained optimisation is setup using the gradient-based *fmincon* optimiser available in MATLAB. Since it was found that multiple pressure profiles resulted in complete evaporation, the objective function was defined as:

$$f(\mathbf{x}) = x_{V,max}\,\frac{L_N}{L|_{x_{V,max}}} \tag{12}$$

where $x_{V,max}$ is either 1 in case of full evaporation or the maximum vapour mass fraction achieved, L_N is the nozzle length, and $L|_{x_{V,max}}$ is the streamwise distance at which the mixture turns to dry vapour or reaches the maximum quality. Maximising $f(\mathbf{x})$ ensures that a pressure profile is found that ensures the quickest wet-to-dry transition. The design variables are the coordinates of the three Bezier control points shown in Fig. 2. Although it was initially planned to include the geometrical ratios, L/o_{th} and b/o_{th} as design variables, both parameters were found to have little effect on the evaporation rate in the quasi-1D code. The insensitivity to the throat height to width ratio can be understood since the 1D equations only solve for the cross-sectional area. However, the insensitivity to the nozzle length is a little more surprising as one might expect a longer nozzle to result in a less rapid expansion of the flow, giving more time for liquid droplets to evaporate. To avoid flow discontinuities at the inlet and outlet, a zero-gradient condition is maintained at the inlet and outlet, which implies that the y-coordinate of the control points cp_1 and cp_3 is fixed at 1 and 0 respectively as shown in Fig. 2. Hence, there are four design variables in total, which include the x-coordinates of all three control points, and the y-coordinate of the middle control point cp_2. Each design variable can take any value between 0 and 1, when expressed in terms of the normalised coordinates (see Fig. 2). However, the resulting profile has to satisfy two constraints. First, the pressure gradient $\mathrm{d}p/\mathrm{d}x$ has to remain negative throughout the expansion, i.e. the pressure must continually decrease. The other constraint was related to the maximum magnitude of the pressure gradient $|\mathrm{d}p/\mathrm{d}x|$, which could not exceed 25 (expressed in terms of non-dimensional coordinates). It was found that pressure profiles with $|\mathrm{d}p/\mathrm{d}x| > 25$ resulted in excessive nozzle curvature. This in turn led to very abrupt expansions associated with flow separation and high energy losses. To avoid ending up at a local minimum, the optimiser was run using 100 randomly generated starting points within the design space.

The results shown in Fig. 11 provide a comparison between the baseline and optimised pressure profiles. In each case, the optimum

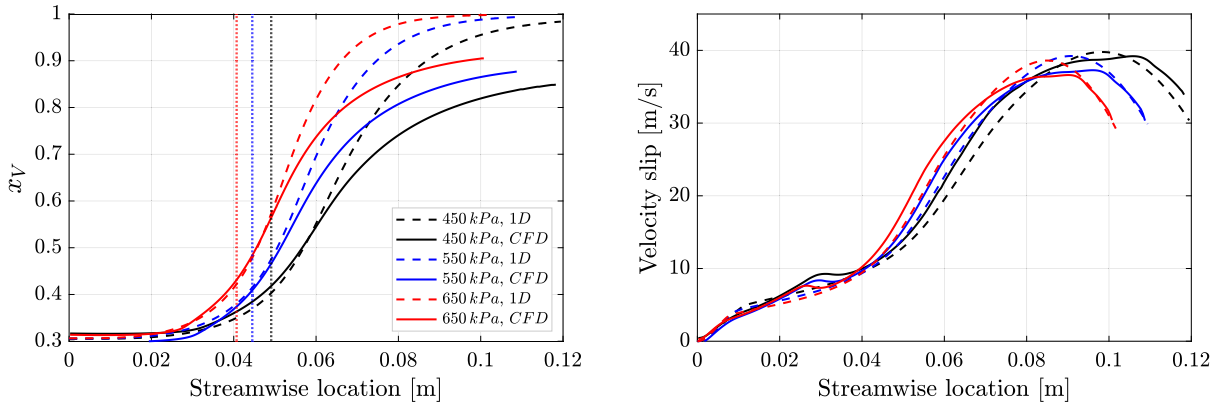

Fig. 10. Comparison of average streamwise variation of vapour mass fraction (left) and velocity slip (right) between the quasi-1D design tool and CFD; the dotted lines represent the throat location.

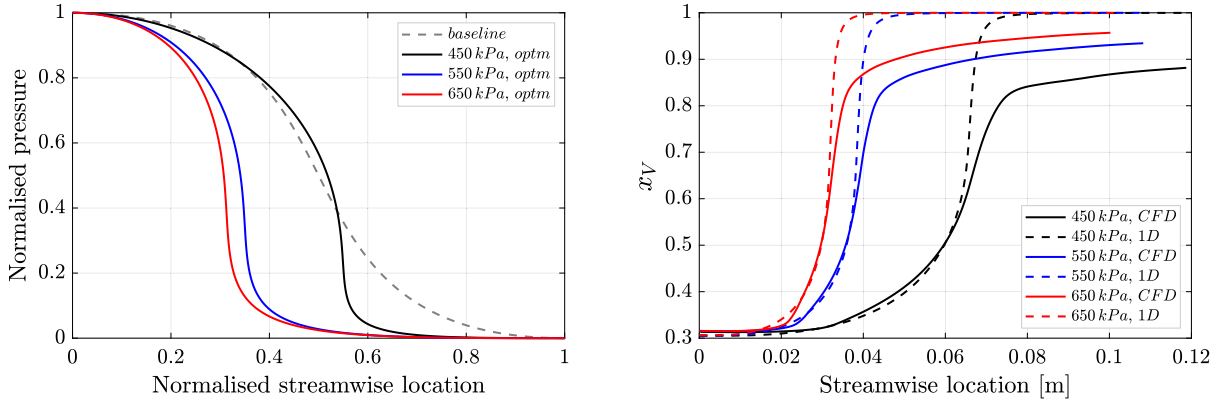

Fig. 11. Optimised pressure profiles (left); comparison of average streamwise variation of vapour mass fraction x_V predicted by the quasi-1D tool and CFD in the optimised geometries (right).

pressure profile reached the maximum allowable gradient of 25. The profiles for 550 and 650 kPa expansions look almost identical, with most of the expansion occurring close to the inlet. This seems logical as the breakup occurs quicker, with the remaining of the expansion occurring with smaller droplets. It is unclear to the authors why the pressure drop occurs further downstream for the 450 kPa expansion, however dry conditions were predicted for that expansion in spite of the throat being shifted downstream. The main reason why a high pressure gradient is optimal is since it brings about a more rapid expansion that promotes a more severe droplet fragmentation and leads to smaller droplet diameters in the diverging section of the nozzle. This occurs due to high flow gradients and the associated aerodynamic disruptive forces acting on the droplet. The post-breakup droplet diameter in nozzles designed with the baseline profile varied between 10.4 and 13.2 μm. This reduced to around 4.34 to 5.57 μm in the optimised nozzles. The smaller the droplet size the larger the interfacial area for a given liquid volume fraction; this in turn directly enhances the rate of interfacial heat transfer rate and consequently interphase mass transfer. The comparison between the design and CFD pressure profiles showed a greater discrepancy near the nozzle outlet in relation to the baseline geometries. Generally, the flow was underexpanded with the outlet pressure being around 9.6% higher than the design value in each investigated case. This could be due to the formation of a shock resulting from a much more rapid expansion in the optimised nozzles, which could not be predicted with the quasi-1D design tool. When it comes to the vapourisation rate, according to the quasi-1D tool, the optimised geometry provide dry outlet conditions in each case and wet-to-dry transition takes place further upstream of the outlet compared to the baseline profile (compare dashed lines in Figs. 10 (left) and 11 (right)).

Although the quasi-1D results look promising, the evaporation may be reduced by the two-dimensional, viscosity and turbulence effects as apparent from Fig. 10. The results in Fig. 11 (right) show a comparison between quasi-1D and CFD predictions of average streamwise variation of x_V for the optimised pressure profiles. First, comparing Figs. 10 to 11, it can be easily noticed that like in the baseline cases, the evaporation rate estimated by CFD is reduced in comparison with the quasi-1D tool prediction, while the overall trends are conserved. Comparing the CFD results of the baseline and optimised geometries in Fig. 12, a visible and consistent improvement in the outlet vapour mass fraction can be observed, which amounts to around 0.04–0.05 increase. The outlet x_V increases from 0.849, 0.877 and 0.905 to 0.882, 0.934 and 0.957 for the 450, 550 and 650 kPa expansions respectively. Although full evaporation was not achieved in any of the investigated cases, the liquid mass fraction at the outlet of the optimised nozzle design for the expansion from 650 kPa dropped below 5%, which is promising. Considering the gradient of the x_V curve near the outlet, it appears that further increase in the outlet x_V could be achieved by elongating the nozzle.

The influence of the pressure profile on the nozzle efficiency and flow uniformity is also important. This could not be directly accounted for in the one-dimensional optimisation due to quasi-1D inviscid flow assumption, but can be assessed from the CFD results. Fig. 12 (right) reports the average streamwise variation of mass-flow averaged entropy of the two-phase mixture (s_{mix}). Generally, the more rapid pressure change that results in the optimised case has a negative effect on the nozzle performance as the total entropy generated increases.

It is worth to mention here, that the authors noticed some non-physical entropy oscillations in previous analyses, with local entropy

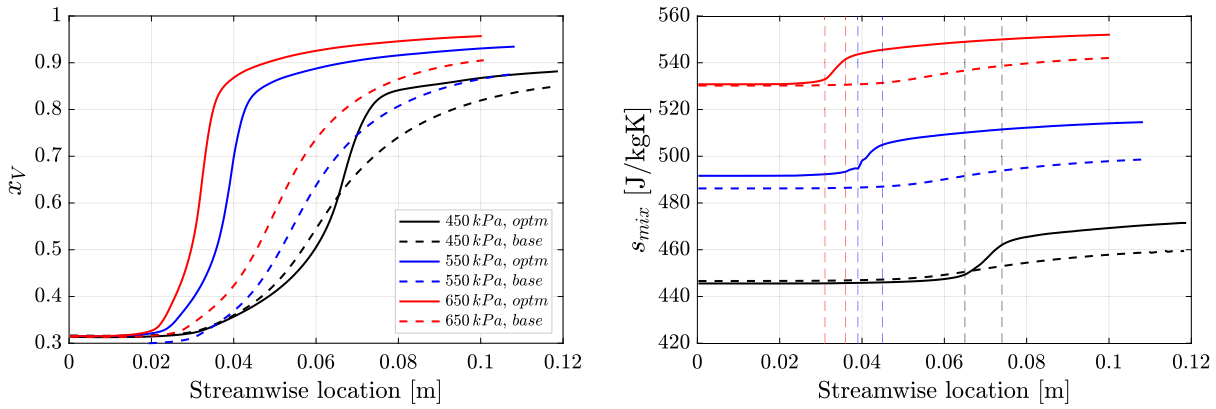

Fig. 12. Comparison of CFD predictions of average streamwise variation of vapour mass fraction (left) and mass-flow average entropy (right) for the baseline and optimised (optm) pressure profiles; dotted lines represent nozzle sections with the most sudden entropy increase.

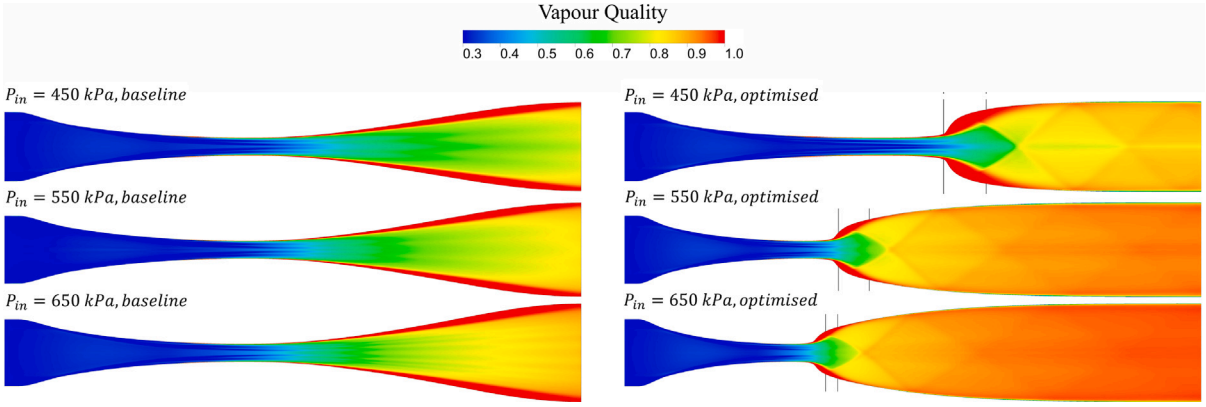

Fig. 13. Two-dimensional contours of vapour quality in the baseline and optimised geometries; dotted lines correspond to the location of the most sudden entropy increase.

drops. This happened in spite of the remaining flow parameters behaving in a physical manner. After some inspection, it was found that this was related to the averaging process rather than to the solution. After placing the transverse planes, used for averaging, across the middle of the grid cells the oscillations disappeared. It is unclear why placing the averaging place at the boundaries of the grid elements, which was done before, caused the issues. To provide a more explicit measure of nozzle performance, the nozzle efficiency was also estimated. The efficiency of the baseline nozzles was 81.09, 81.65 and 84.25% for the 450, 550 and 650 kPa expansion respectively. The efficiency dropped to 67.58, 74.98 and 78.42% for the optimised geometries, which is in line with the average entropy curves (Fig. 12).

The two-dimensional contours of vapour quality as predicted by the CFD simulations are reported in Fig. 13, which help to reveal the flow's spatial uniformity, and shed more light on the flow behaviour and the cause of the sudden rise in generated entropy. What appears to be common in all cases, is the phase separation in the diverging section of the nozzle. This is due to much higher liquid density and high droplet relaxation times, which cannot immediately adjust to the changing geometry in an accelerating flow field. This becomes evident when assessing the liquid streamlines shown in Fig. 14, which are plotted for the baseline nozzle designed for the expansion from an inlet pressure of 550 kPa and an inlet vapour quality of 0.3. It is clear that the droplets are not capable of immediately adjusting their flow direction to the changing nozzle geometry. This leads to an accumulation of the liquid phase near the wall in the converging section of the nozzle, while it remains closer to the nozzle centre downstream of the throat, creating a characteristic core flow. As a result, in the vicinity of the wall in the diverging section the flow is primarily occupied by the vapour phase.

Another phenomenon common to all the investigated geometries is the presence of peculiar alternating strips of varying vapour quality, which is particularly visible near the throat of the nozzle. Further investigation revealed that the alternative strips are the consequence of the lift force that tends to shift the droplets in the lateral direction. Fig. 15 illustrates the difference in the liquid streamlines in the proximity of the throat predicted by CFD simulations ran with and without the lift force included.

With the lift force turned off, the simulation predicts a layer of highly concentrated liquid at the nozzle wall, which appears to be the result of droplets impinging onto the wall in the converging section. Because of this impingement, a layer of high void fraction is developed between the liquid at the wall and the core of the nozzle. As for the nozzle core itself, a fairly uniform liquid distribution was observed. When the lift force is introduced, a similar liquid layer was observed at the wall in the early stage of expansion. However, as the mixture advances downstream, the droplets that are concentrated at the wall are repelled towards the centre of the nozzle due to the lift effects. On the other hand, the droplets flowing along the centreline seem to be shifted towards the wall. As a result, the lift force leads to multiple stratification layers which are in line with the non-uniform variations of vapour quality illustrated in Fig. 13. At this point it is important to mention that previous studies on flash boiling of water demonstrated difficulties in accurate prediction of vapour bubble distribution within the studied channels [15,17,19]. Although polydispersed simulations were conducted with a suitable estimation of the bubble size distribution, the lateral (radial) distribution of bubbles observed experimentally could not be accurately reproduced in the CFD simulation [19]. This could point to the limitations and inaccuracies of the current lift and turbulent dispersion models [19]. With that being said, as far as the bulk flow properties are concerned, the results obtained with and without the lift force include did not deviate drastically. The

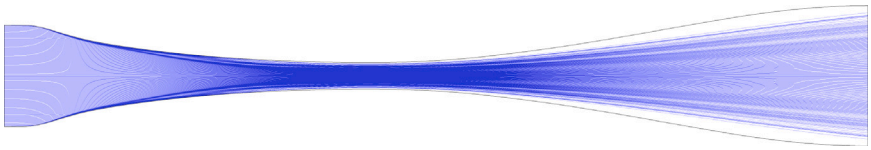

Fig. 14. Liquid streamlines plotted for the baseline nozzle designed for the expansion from an inlet pressure of 550 kPa and an inlet vapour quality of 0.3.

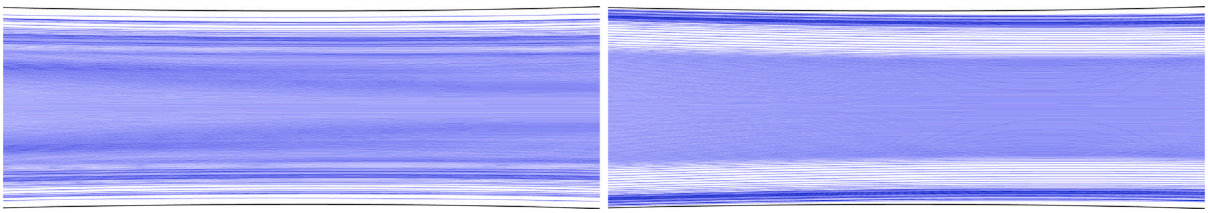

Fig. 15. Liquid streamlines in the proximity of the nozzle throat predicted by the baseline CFD model (left) and a CFD model with the lift force turned off (right); the figure was plotted for the baseline nozzle designed for the expansion from an inlet pressure of 550 kPa and an inlet vapour quality of 0.3.

relative difference in vapour mass fraction at the outlet and the mass-flow rate was below 2.5%, while the difference in the estimated nozzle efficiency did not exceed 3%.

Generally, the flow-field looks very similar in each baseline geometry. Comparing the baseline and optimised nozzles, the phase separation in the diverging section seems to be alleviated to some extent. Nevertheless, an oblique shock train appears to form in the optimised nozzles shortly downstream of the throat, which eventually causes entropy generation and performance loss. It should be noted here that the contours illustrate the variation of vapour quality derived from the local volume fraction values multiplied by the corresponding densities of liquid and vapour. The formulation based on the ratio of mass flow rates (i.e., x_V) could not be displayed in the contours as it is calculated across planes perpendicular to the main flow direction. This also explains why there is a sudden increase in vapour quality across the shock, which is a result of the density variations of the liquid and vapour phases across the shock and is not necessarily associated with an instantaneous vapourisation across the shock. Essentially, the vapour phase experiences a much higher density increase across the shock relative to the liquid phase, which causes the quality to increase despite the volume fraction remaining nearly constant. Although, it could be more appropriate to illustrate the volume fraction contours, it was found that its value was very close to unity, and it could not illustrate the phase change process effectively. With this in mind, the vapour quality definition based on the volume fraction and density values is a useful illustration of the evaporation process including an assessment of any occurring shocks, as long as one keeps in mind that it also reflects sudden density changes. The dotted lines from Fig. 12 are also shown on the contours in the form of thin transverse lines. These indicate the regions of where there a large entropy generation occurs in the nozzle. It can be observed that the location of the sudden rise in s_{mix} can be linked to the location of abrupt geometry change and the resulting onset of the oblique shock train. Looking at the optimised geometries, the most abrupt flow area change occurs for the 450 kPa expansion, which is why it experiences the largest efficiency drop - more than 13.5% lower compared to 5.8% for the 650 kPa expansion. In summary, the optimised nozzles could increase the outlet vapour mass fraction and reduce the extent of lateral phase separation providing a more uniform flow at the outlet, but they were also characterised by less efficient expansion due to the formation of an oblique shock.

5. CFD-based shape optimisation

The influence of lateral flow variations, the formation of shock waves, and viscosity effects on the nozzle performance highlights the limitation of using the quasi-1D nozzle design tool for nozzle optimisation. In fact, the nozzle design tool was initially developed as a means to design shock-free nozzles for wet-to-dry nozzles, and as such is not capable of predicting or accounting for the presence of shock waves in the nozzle. Nonetheless, the optimisation study completed using this tool was considered a useful exercise to assess the influence of the pressure profile on the vaporisation rate. The results from the study also highlights the important trade-off between maximising vapour generation rate and minimising entropy production which are both important factors for a turbine intended for a wet-to-dry cycle. Whilst the nozzle design tool could be modified to account for shock and viscous losses, a preferred option is to carry out CFD-based shape optimisation. With this in mind, this section details a shape optimisation study for one of the expansion cases, with the aim of highlighting the potential to further improve performance of the nozzle.

5.1. Optimisation setup

For this shape optimisation study, only the expansion case from 550 kPa and inlet quality of 0.3 was investigated. The results of the one-dimensional optimisation demonstrated that the area of the most importance was the region located directly downstream of the throat. As such, it was decided to simplify the problem and focus only on optimising the shape of the nozzle around that location. The optimisation was implemented within Ansys Workbench, which provides a framework that combines the geometry, meshing, solution, and optimisation modules.

The wall profile obtained from the 1D optimisation was first parameterised, using a spline with 20 geometry points, as illustrated in Fig. 16. The shape of the converging section was kept fixed, while the optimisation focused only on the area near the throat, which has the greatest impact on the flow and phase change process. As such, only two of the geometry points, gp_1 and gp_2, marked with red circles in Fig. 16, are set as design variables. However, the remaining geometry points in the diverging section are adjusted according to the position of the two geometry points to ensure a smooth and continuous increase in the flow area. The length of the nozzle, and the horizontal position of all the points is fixed, while the vertical position of gp_1 and gp_2 is varied during the optimisation. To ensure the mass-flow rate remains approximately the same, the throat height was fixed at 3.422 mm. Since the distance from the centreline to the wall at the throat was 1.711 mm, the range of vertical motion of the first point, y_{gp_1}, was set between 2.25 and 5.25 mm. This range was found to be sufficient to simulate nozzles with various expansion rates ranging from gradual to very rapid. The vertical position of the second point, y_{gp_2}, was controlled indirectly through the following non-dimensional parameters:

$$c_1 = 0.1 + 0.15\left(y_{gp_1} - 2\right) \tag{13a}$$

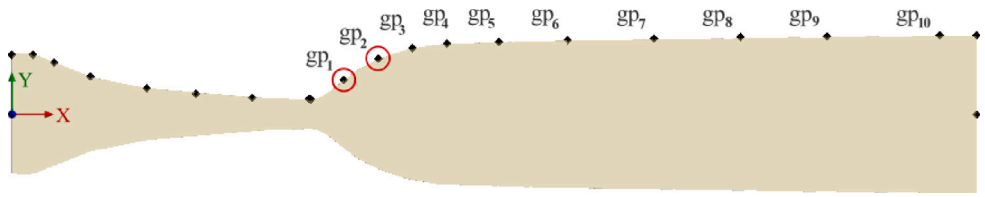

Fig. 16. The parametrisation of the nozzle used in shape optimisation.

$$c_2 = \left(\frac{y_{gp_1}}{9} + \frac{4\left(y_{gp_1} - 2.25\right)}{45} \right) k \tag{13b}$$

$$c_3 = c_1 + c_2\left(0.90 - c_1\right) \tag{13c}$$

The vertical position of gp_2 is then expressed as:

$$y_{gp_2} = y_{gp_1} + c_3(y_{out} - y_{gp_1}) \tag{14}$$

where y_{out} is the outlet height, measured from the centreline of the nozzle. These relationships were derived based on trial and error, which involved investigating a suitable range of motion of y_{gp_2} for various positions of gp_1. Generally, the vertical position of gp_1 should control the rate of expansion within the nozzle. In other words, if y_{gp_1} was relatively small, the resulting expansion should be gradual. Therefore, y_{gp_2} had to be limited if y_{gp_1} was small in order to achieve a gradual expansion. Otherwise the expansion would only be shifted longitudinally from gp_1 to gp_2. Moreover, the maximum gradient of the wall profile was to take place between the throat and gp_1 and should gradually streamwise. These considerations were taken into account when developing the relationships for the vertical position of geometry points gp_2 through gp_{10}. Looking at Eq. (13a)–(13c), it can be seen that for any value of y_{gp_1}, y_{gp_2} depends only on the parameter k from Eq. (13b). This parameter was the second design variable in the optimisation, which varied between 0 and 1, controlling the range of motion of gp_2 relative to gp_1. Although the remaining points in the diverging section were not used as optimisation inputs, a set of correlations was developed through trial and error and based on the considerations mentioned above:

$$y_{gp_3} = y_{gp_2} + c_3(y_{out} - y_{gp_2}) \tag{15a}$$

$$y_{gp_4} = y_{gp_3} + \left(0.15 + 0.1(y_{gp_3} - 2.25) + 0.1k\right)(y_{out} - y_{gp_3}) \tag{15b}$$

$$y_{gp_5} = y_{gp_4} + 0.2(y_{out} - y_{gp_4}) \tag{15c}$$

$$y_{gp_6} = y_{gp_5} + 0.25(y_{out} - y_{gp_5}) \tag{15d}$$

$$y_{gp_7} = y_{gp_6} + 0.2333(y_{out} - y_{gp_6}) \tag{15e}$$

$$y_{gp_8} = y_{gp_7} + 0.5(y_{out} - y_{gp_7}) \tag{15f}$$

$$y_{gp_9} = y_{gp_8} + 0.5(y_{out} - y_{gp_8}) \tag{15g}$$

$$y_{gp_{10}} = y_{out} \tag{15h}$$

The mesh with 15,000 elements, described in Section 3.2.2, was used in CFD evaluations, which gave a good balance between accuracy and simulation time. The CFD simulations were performed using the same setup as described previously. The construction of the initial database and sampling of the design space was performed using optimal-space filling, a variant of Latin Hypercube technique, which was capable of uniformly resolving the design space with 55 design points. The response surface was constructed using a genetic aggregation technique, but due to the simplicity of the problem and the smoothness of the response, other existing methods could potentially generate an equally reliable approximation. The accuracy of the response surface was assessed with 10 verification points, comparing the response surface approximations for the outlet vapour mass fraction and the nozzle efficiency against the CFD evaluations. The maximum relative difference was below 0.11% and 0.36% for the vapour mass fraction and the nozzle efficiency, respectively, which was considered sufficiently small. To carry out the optimisation of the response surface, a multi-objective genetic algorithm, non-dominated sorting genetic algorithm (NSGA-II), was used which aimed to simultaneously maximise the outlet vapour mass fraction and nozzle efficiency.

Table 4
The results of shape optimisation study.

Case	y_{gp_1}	y_{gp_2}	$x_{V,out}$	η_N
Run 1	3.973 mm	6.111 mm	0.941	76.19%
Run 2	3.452 mm	5.261 mm	0.935	77.96%
1D Optimal	–	–	0.934	74.98%

5.2. Shape optimisation results

Based on the evaluation of the 55 design points used to create the initial database, the range of outlet vapour mass fractions and nozzle efficiencies were assessed. The outlet vapour mass fraction varied between 0.915 and 0.951, which was considered a relatively narrow range. Comparing these values to $x_{V,out}$ of the 1D-optimised nozzle for the 550 kPa expansion, which was 0.934, the potential increase in the evaporation rate appears fairly small. Furthermore, the highest $x_{V,out}$ values corresponded to very low nozzle efficiencies. Contrary to the vapour mass fraction, the efficiency variation was substantially larger, ranging from 64.59 to 81.35%. Since the efficiency of the 1D-optimised nozzle was 74.98%, this indicates there is significant room for performance improvement. Considering the results for the initial database, two optimisation runs were carried out. In the first run, a multi-objective optimisation was carried out to simultaneously maximise both the vapourisation rate and efficiency, while in the second run a single-objective optimisation of the nozzle efficiency was carried with a constraint set such that $x_{V,out} > 0.934$. In theory, the optimal nozzle design with an outlet vapour quality of 0.934 could have been retrieved directly from the Pareto front generated by the multi-objective optimisation, but this second run was considered to verify that there was no further room for improvement. Moreover, in this second case, the optimised geometry would at least provide the same outlet vapour mass fraction as the 1D-optimised nozzle and enable a direct comparison. Several candidate points were generated in both runs, which were then verified with the CFD model. The results of both runs are shown in Table 4 alongside the one-dimensional optimisation results as reference.

In the first run of the optimisation (Run 1), the optimiser was set to simultaneously enhance the evaporation rate and efficiency, while the optimal solution was generated applying equal weighting factors to both parameters. The optimised nozzle achieved 0.007 higher outlet vapour mass fraction and about 1.2% higher efficiency compared to the 1D-optimised nozzle. However, when the optimiser was set to search for the maximum efficiency, while maintaining $x_{V,out} > 0.934$ (Run 2), the resulting geometry yielded a 3% increase in efficiency at an expense of a slightly smaller value for $x_{V,out}$. Since $x_{V,out}$ in the second run was only marginally smaller, the geometry obtained in Run 2 was considered as the optimal nozzle design. Two-dimensional contours of vapour quality for the 1D-optimised nozzle, and the one obtained through shape optimisation (2D-optimised) are compared in Fig. 17.

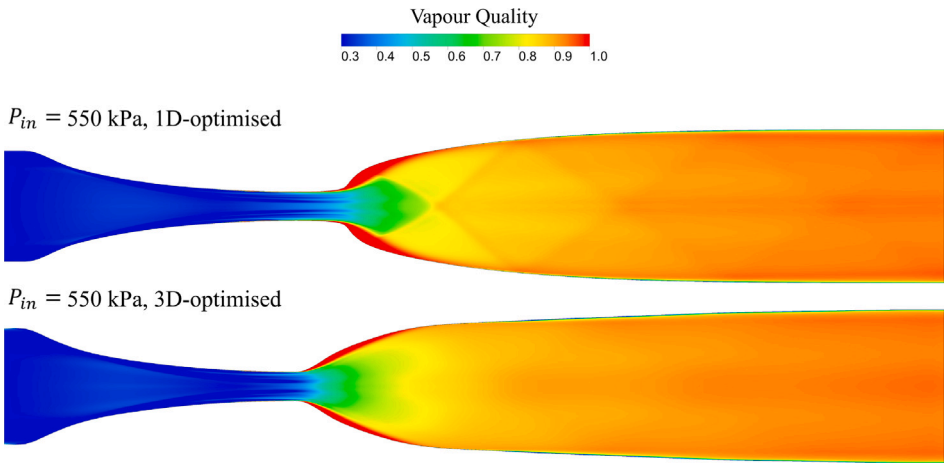

Fig. 17. Two-dimensional contours of vapour quality in the 1D-optimised and 2D-optimised geometries.

It can be observed that the 2D-optimised geometry facilitates a more gradual expansion, mitigating the negative effects of the oblique shock train that was observed in the 1D-optimised geometry. This results in reduced energy losses and a 3% increase in efficiency. In conclusion, despite being unable to significantly enhance the vapourisation rate, the shape optimisation was successful at generating a geometry that mitigated the problem of an oblique shock train, leading to a higher expansion efficiency.

5.3. Effect of other geometrical parameters

According to the quasi-1D design tool, the influence of passage height and nozzle length on the evaporation rate is negligible. However, the design tool does not account for viscosity effects, which could be expected to vary with geometrical parameters such as throat height. In order to assess the importance of the height of the passage and nozzle length, a preliminary analysis was conducted on the 2D-optimised geometry Fig. 17 from the previous section. To vary the passage height, the vertical distance from the centreline for each geometry point shown in Fig. 16 was multiplied by a factor of 0.5 and 2. To maintain the same wall profile and thereby the expansion rate, the horizontal distance between the consecutive geometry points was also multiplied by a factor of 0.5 or 2 accordingly. When it comes to the effect of nozzle length, the vertical position of all the geometry points was kept fixed, while the horizontal distance between the consecutive geometry points in the diverging section, starting with the 6th point downstream of the throat (Fig. 16), was multiplied by a factor of 2 and 0.5. This ensured almost the same expansion rate, while only elongating the straight diverging section of the nozzle.

The effect of passage width on the vapourisation rate was found to be rather small with a maximum difference of 0.01 compared to the original 2D-optimised geometry. As for the efficiency, the smaller width, characterised by a narrower throat, induced a 3.3% efficiency loss, which is thought to be the result of increased viscous losses in the throat area. The reverse happened for the wider passage, which was associated with an efficiency increase of about 2.2%. As expected, the mass-flow rate within the nozzle with height multiplied by a factor of 0.5 was around 51.7% lower, while for the nozzle with doubled throat height it was around 196% higher. The length of the nozzle had a slightly higher impact on the outlet vapour mass fraction, which reached 0.952 and 0.912 for the longer and shorter nozzles respectively. The difference in efficiency was around 1%, with the shorter nozzle having a higher efficiency due to reduced viscous losses. Although the channel width and nozzle length do not drastically alter the overall characteristics of the two-phase expansion (as far as the vapour quality and velocity contours are concerned), these parameters may considerably affect the vapourisation rate and efficiency if combined with the optimisation of the nozzle shape. Therefore, the authors plan to conduct further shape optimisation studies in future, accounting for the combined effect of expansion rate, passage width and nozzle length, alongside considering other operating conditions and three-dimensional simulations accounting for the endwall effects.

6. Conclusions

In this study, the geometry of converging-diverging nozzles for the wet-to-dry expansion of organic fluids has been studied using a combination of a quasi-1D non-equilibrium design tool and non-equilibrium quasi-2D CFD simulations. Three expansions with inlet pressure ranging from 450 to 650 kPa and constant inlet vapour quality of 0.3 were investigated for the siloxane MM. First, pressure profile optimisation was carried out using the nozzle design tool to maximise the vapourisation rate. The optimised geometries were simulated using a CFD model that accounted for viscosity, turbulence and two-dimensional effects. In the second part of the study, CFD-based shape optimisation was also carried out, focusing on optimising the near-throat area, which has the greatest impact on the expansion.

It was found that the quasi-1D nozzle design tool is capable of predicting the phase-change pattern, but the assumption of inviscid quasi-1D flow and the omission of viscous and turbulence effects leads to an over-prediction in the evaporation rate. However, since the phase-change pattern predicted by the quasi-1D tool is similar to the non-equilibrium CFD predictions, the tool was still deemed suitable for performing initial 1D optimisation. It was found that the optimised nozzles resulted in a rapid expansion that enhanced the droplet breakup and consequently the vapourisation rate. The CFD simulations conducted on the geometries generated using the optimised pressure profiles achieved 3.3 to 5.7% higher vapour mass fraction at the outlet, which reached 88.2, 93.4 and 95.7% for the expansions from 450, 550 and 650 kPa respectively. Although complete evaporation was achieved in none of the cases, reaching near-dry conditions for inlet pressures in the order of 650 kPa seems promising. Evaluation of the flow-field revealed that the abrupt expansion in the optimised geometries was associated with the formation of an oblique shock train downstream of the throat, which in turn contributed to elevated entropy generation. The nozzle efficiencies for the optimised geometries were in the range of 67.58 to 78.42%, approximately 5.8 to 13.5% lower compared to the baseline geometries, with more pronounced loss at low pressures. This

highlights the limitation of using the quasi-1D inviscid nozzle design tool for nozzle optimisation, and highlights the need for multi-objective optimisation using more advanced simulation methods.

As such, CFD-based shape optimisation studies aimed at maximising the outlet vapour mass fraction and nozzle efficiency, were conducted. The results revealed that by optimising the wall profile near the throat, it was possible to design a nozzle that achieves a similar vapourisation rate to that of the 1D-optimised geometry, while facilitating more efficient expansion. The 2D-optimised nozzle facilitated a more gradual expansion, mitigating the negative effects of the oblique shock train appearing in the 1D-optimised geometry, leading to a 3% increase in nozzle efficiency, which reached around 78%.

The CFD-based shape optimisation study focused only on refining the nozzle area in close vicinity to the throat. However, other geometrical parameters, such as passage width and nozzle length, which have been shown to influence the expansion, were not taken into account. More comprehensive shape optimisation study is planned to be conducted in future, further expanding the approach to include these aspects.

Declaration of competing interest

The authors declare that they have no known competing financial interests or personal relationships that could have appeared to influence the work reported in this paper.

Acknowledgements

This project was supported by the Royal Academy of Engineering, United Kingdom under the Research Fellowship scheme (2019–2024). Award number: RF\201819\18\23. The authors would also like to express gratitude towards City, University of London for funding the Ph.D. studentship of Mr Pawel Ogrodniczak.

Data availability

Data will be made available on request.

References

[1] C. Wieland, C. Schifflechner, K. Braimakis, F. Kaufmann, F. Dawo, S. Karellas, G. Besagni, C.N. Markides, Innovations for organic Rankine cycle power systems: Current trends and future perspectives, Appl. Therm. Eng. 225 (2023) 120201, http://dx.doi.org/10.1016/j.applthermaleng.2023.120201.

[2] M.T. White, Cycle and turbine optimisation for an ORC operating with two-phase expansion, Appl. Therm. Eng. 192 (2021) 116852, http://dx.doi.org/10.1016/j.applthermaleng.2021.116852.

[3] G. Lhermet, N. Tauveron, N. Caney, Q. Blondel, F. Morin, A recent advance on partial evaporating organic Rankine cycle: Experimental results on an axial turbine, Energies 15 (20) (2022) 7559, http://dx.doi.org/10.3390/en15207559.

[4] Y. Liao, D. Lucas, Computational modelling of flash boiling flows: A literature survey, Int. J. Heat Mass Transfer 111 (2017) 246–265, http://dx.doi.org/10.1016/j.ijheatmasstransfer.2017.03.121.

[5] N. Abuaf, B.J. Wu, G.A. Zimmer, P. Saha, Study of nonequilibrium flashing of water in a converging-divergingnozzle. volume 1: Experimental, Brookhaven National Laboratory, 1981.

[6] Z. Blicki, J. Kestin, Physical aspects of the relaxation model in two-phase flow, Proc. R. Soc. A 428 (1990) 379–397, http://dx.doi.org/10.1098/rspa.1990.0040.

[7] P. Downar-Zapolski, Z. Bilicki, L. Bolle, J. Franco, The non-equilibrium relaxation model for one-dimensional flashing liquid flow, Int. J. Multiph. Flow 22 (3) (1996) 473–483, http://dx.doi.org/10.1016/0301-9322(95)00078-X.

[8] W. Angielczyk, Y. Bartosiewicz, D. Butrymowicz, J.-M. Seynhaeve, 1-D modeling of supersonic carbon dioxide two-phase flow through ejector motive nozzle, in: International Refrigeration and Air Conditioning Conference, Purdue, France, 2010.

[9] M. Palacz, M. Haida, J. Smolka, A.J. Nowak, K. Banasiak, A. Hafner, HEM and HRM accuracy comparison for the simulation of CO2 expansion in two-phase ejectors for supermarket refrigeration systems, Appl. Therm. Eng. 115 (2017) 160–169, http://dx.doi.org/10.1016/j.applthermaleng.2016.12.122.

[10] M. Loska, J. Smolka, M. Haida, E.E. Kriezi, K. Banasiak, CFD modelling of R410A flow through an expansion valve using equilibrium and modified relaxation models, Appl. Therm. Eng. 185 (2021) 116442, http://dx.doi.org/10.1016/j.applthermaleng.2020.116442.

[11] M. De Lorenzo, P. Lafon, J.-M. Seynhaeve, Y. Bartosiewicz, Benchmark of delayed equilibrium model (DEM) and classic two-phase critical flow models against experimental data, Int. J. Multiph. Flow 92 (2017) 112–130, http://dx.doi.org/10.1016/j.ijmultiphaseflow.2017.03.004.

[12] C. Tammone, A. Romei, F. Persico, Extension of the delayed equilibrium model to flashing flows of organic fluids in converging-diverging nozzles, Int. J. Multiph. Flow 171 (2024) 104661, http://dx.doi.org/10.1016/j.ijmultiphaseflow.2023.104661.

[13] P. Ogrodniczak, M.T. White, Non-equilibrium CFD simulation of the wet-to-dry expansion of the siloxane MM in a converging–diverging nozzle, Appl. Therm. Eng. 234 (2023) 121158, http://dx.doi.org/10.1016/j.applthermaleng.2023.121158.

[14] Y. Liao, D. Lucas, E. Krepper, R. Rzehak, CFD simulation of flashing boiling flow in the containment cooling condensers (CCC) system of KERENA^{TM} reactor, in: Proceedings of the 2013 21st International Conference on Nuclear Engineering, ICONE21, Chengdu, China, 2013.

[15] Y. Liao, D. Lucas, 3D CFD simulation of flashing flows in a converging-diverging nozzle, Nucl. Eng. Des. 292 (2015) 149–163, http://dx.doi.org/10.1016/j.nucengdes.2015.06.015.

[16] S. Mimouni, M. Boucker, J. Laviéville, A. Guelfi, D. Bestion, Modelling and computation of cavitation and boiling bubbly flows with the NEPTUNE_CFD code, Nucl. Eng. Des. 238 (3) (2008) 680–692, http://dx.doi.org/10.1016/j.nucengdes.2007.02.052.

[17] J.P. Janet, Y. Liao, D. Lucas, Heterogeneous nucleation in CFD simulation of flashing flows in converging-diverging nozzles, Int. J. Multiph. Flow 74 (2015) 106–117.

[18] C. Marsh, A. O'Mahony, Three-dimensional modelling of industrial flashing flows, Prog. Comput. Fluid Dyn. Int. J. 9 (6/7) (2009) 393, http://dx.doi.org/10.1504/PCFD.2009.027370.

[19] Y. Liao, D. Lucas, Possibilities and limitations of CFD simulation for flashing flow scenarios in nuclear applications, Energies 10 (1) (2017) http://dx.doi.org/10.3390/en10010139.

[20] E. Ortego Sampedro, F. Breque, M. Nemer, Two-phase nozzles performances CFD modeling for low-grade heat to power generation: mass transfer models assessment and a novel transitional formulation, Therm. Sci. Eng. Prog. (2021) 101139.

[21] J. Zhu, S. Elbel, Measurement of static pressure profiles of vortex flashing R134a flow expanded through convergent–divergent nozzles, Int. J. Refrig. 108 (2019) 258–270, http://dx.doi.org/10.1016/j.ijrefrig.2019.08.023.

[22] J. Zhu, S. Elbel, CFD simulation of vortex flashing R134a flow expanded through convergent-divergent nozzles, Int. J. Refrig. 112 (2020) 56–68, http://dx.doi.org/10.1016/j.ijrefrig.2019.12.005.

[23] M.T. White, Investigating the wet-to-dry expansion of organic fluids for power generation, Int. J. Heat Mass Transfer 192 (2022) 122921, http://dx.doi.org/10.1016/j.ijheatmasstransfer.2022.122921.

[24] D. Pasquale, A. Ghidoni, S. Rebay, Shape optimization of an organic Rankine cycle radial turbine nozzle, J. Eng. Gas Turbines Power 135 (4) (2013) 042308.

[25] G. Persico, Evolutionary optimization of centrifugal nozzles for organic vapours, J. Phys. Conf. Ser. 821 (2017) 012015, http://dx.doi.org/10.1088/1742-6596/821/1/012015.

[26] G. Persico, A. Romei, V. Dossena, P. Gaetani, Impact of shape-optimization on the unsteady aerodynamics and performance of a centrifugal turbine for ORC applications, Energy 165 (2018) 2–11, http://dx.doi.org/10.1016/j.energy.2018.09.044.

[27] A.M. Al Jubori, R. Al-Dadah, S. Mahmoud, Performance enhancement of a small-scale organic Rankine cycle radial-inflow turbine through multi-objective optimization algorithm, Energy 131 (2017) 297–311.

[28] A.L. Espinosa Sarmiento, R.G. Ramirez Camacho, W. de Oliveira, E.I. Gutiérrez Velásquez, M. Murthi, N.J. Diaz Gautier, Design and off-design performance improvement of a radial-inflow turbine for ORC applications using metamodels and genetic algorithm optimization, Appl. Therm. Eng. 183 (2020) (2021).

[29] A.S. Abdeldayem, M.T. White, A. Paggini, M. Ruggiero, A.I. Sayma, Integrated aerodynamic and structural blade shape optimization of axial turbines operating with supercritical carbon dioxide blended with dopants, J. Eng. Gas Turbines Power 144 (10) (2022) 101016, http://dx.doi.org/10.1115/1.4055232.

[30] W.E. Ranz, W.R. Marshall Jr., Evaporation from drops: Part 1, Chem. Eng. Prog. 48 (3) (1952) 141–146.

[31] RELAP5/MOD3 Code Manual Volume: Models and Correlations, Tech. Rep. NUREG/CR-5535-VOL.4, Idaho National Engineering Laboratory, 1995.

[32] G. Brown, Heat Transmission by Condensation of Steam on a Spray of Water Drops (Ph.D. thesis), University of London (Imperial College of Science and Technology), 1948.

[33] M. Ishii, N. Zuber, Drag coefficient and relative velocity in bubbly, droplet or particulate flows, AIChE J. 25 (5) (1979) 843–855.

[34] D. Legendre, J. Magnaudet, The lift force on a spherical bubble in a viscous linear shear flow, J. Fluid Mech. 368 (1998) 81–126.

[35] D.R. Guildenbecher, C. López-Rivera, P.E. Sojka, Secondary atomization, Exp. Fluids 46 (3) (2009) 371–402, http://dx.doi.org/10.1007/s00348-008-0593-2.
[36] O.A. Gobyzov, M.N. Ryabov, A.V. Bilsky, Study of deformation and breakup of submillimeter droplets' spray in a supersonic nozzle flow, Appl. Sci. 10 (18) (2020) 6149, http://dx.doi.org/10.3390/app10186149.
[37] E.W. Lemmon, I.H. Bell, M.L. Huber, M.O. McLinden, NIST Standard Reference Database 23: Reference Fluid Thermodynamic and Transport Properties-REFPROP, Version 10.0, orgname=National Institute of Standards and Technology, 2018, https://www.nist.gov/srd/refprop.
[38] ANSYS CFX, Release 2021 R1, ANSYS Inc..
[39] CFX-Solver Theory Guide, Release 2021 R1, ANSYS Inc..
[40] A. Tomiyama, Struggle with computational bubble dynamics, in: Proceedings of Third International Conference on Multiphase Flow, Lyon, France, 1998.
[41] D.G. Elliott, E. Weinberg, Acceleration of Liquids in Two-Phase Nozzles, Tech. Rep., Jet Propulsion Laboratory, California Institute Of Technology, 1968.
[42] P. Ogrodniczak, M.T. White, Numerical validation of a two-phase nozzle design tool based on the two-fluid model applied to wet-to-dry expansion of organic fluids, in: M. White, T. El Samad, I. Karathanassis, A. Sayma, M. Pini, A. Guardone (Eds.), Proceedings of the 4th International Seminar on Non-Ideal Compressible Fluid Dynamics for Propulsion and Power, Springer Nature Switzerland, 2023, pp. 103–113, http://dx.doi.org/10.1007/978-3-031-30936-6_11.